Title

Chip-scale plasmonic resonant nanostructures : manipulation of light from nano to micro scale

Permalink

https://escholarship.org/uc/item/2k18h8mc

Author

Feng, Liang

Publication Date

2010

Peer reviewed|Thesis/dissertation

UNIVERSITY OF CALIFORNIA, SAN DIEGO

Chip-Scale Plasmonic Resonant Nanostructures: Manipulation of Light from Nano to

Micro Scale

A dissertation submitted in partial satisfaction of the requirements

for the degree Doctor of Philosophy

in

Electrical Engineering (Photonics)

by

Liang Feng

Committee in charge

    Professor Yeshaiahu Fainman, Chair
    Professor Vitaliy Lomakin, Co-Chair
    Professor Sungho Jin
    Professor Zhaowei Liu
    Professor Lu Jeu Sham

2010

The dissertation of Liang Feng is approved, and it is acceptable in quality and form for publication on microfilm and electronically:

_____

_____

_____

_____
                                                        Co-Chair

_____
                                                           Chair

University of California, San Diego

2010

Dedication

To my family, friends, and colleagues,

I am deeply indebted for your inspiration, support, encouragement and considerations. Without all of you, the success of this project and the completion of this thesis would not be possible.

Table of Contents

List of Figures

List of Tables

Acknowledgements

The text of Chapter 3, in part or in full, is a reprint of the material as it appears in the Applied Physics Letters. The dissertation author was the primary researcher and author, and the co-authors listed in this publication directed and supervised the research which forms the basis for this chapter.

The text of Chapter 4, in part or in full, is a reprint of the material as a recent submission. The dissertation author was the primary researcher and author, and the co-authors listed in this publication directed and supervised the research which forms the basis for this chapter.

The text of Chapter 5, in part or in full, is a reprint of the material as it appears in the Applied Physics Letters. The dissertation author was the primary researcher and author, and the co-authors listed in this publication directed and supervised the research which forms the basis for this chapter.

The text of Chapter 6, in part or in full, is a reprint of the material as it appears in the Applied Physics Letters. The dissertation author was the primary researcher and author, and the co-authors listed in this publication directed and supervised the research which forms the basis for this chapter.

The text of Chapter 7, in part or in full, is a reprint of the material as it appears in the Optics Express. The dissertation author was the primary researcher and author, and the co-authors listed in this publication directed and supervised the research which forms the basis for this chapter.

VITA

1998~2002   Bachelor of Science in Physics department from Nanjing University, China

2002~2005   Master of Science in Physics department from Nanjing University, China

2005~2010   Doctor of Philosophy in Electrical Engineering (Photonics) from University of California, San Diego

PUBLICATIONS

Liang Feng, Amit Mizrahi, Steve Zamek, Zhaowei Liu, Vitaliy Lomakin, and Yeshaiahu Fainman, "Metamaterials for Extraordinary Polarization Conversion in Plasmonic Excitation," submitted.

Liang Feng, Zhaowei Liu, Vitaliy Lomakin, and Yeshaiahu Fainman, "Form Birefringence Metal and Its Plasmonic Anisotropy," Applied Physics Letters **96,** 041112 (2010).

Liang Feng, Derek Van Orden, Maxim Abashin, Qian-Jin Wang, Yan-Feng Chen, Vitaliy Lomakin, and Yeshaiahu Fainman, "Nanoscale Optical Field Localization by Resonantly Focused Plasmons," Optics Express **17**, 4824-4832 (2009).

Liang Feng, Ming-Hui Lu, Vitaliy Lomakin, and Yeshaiahu Fainman, "Plasmonic Photonic Crystal with a Complete Bandgap for Surface Plasmon Polariton Waves," Applied Physics Letters **93,** 231105 (2008).

Liang Feng, Kevin A. Tetz, Boris Slutsky, Vitaliy Lomakin, and Yeshaiahu Fainman, "Fourier Plasmonics: Diffractive Focusing of in-Plane Surface Plasmon Polariton Waves," Applied Physics Letters **91,** 081101 (2007).

Maziar P. Nezhad, Aleksandar Simic, Olesya Bondarenko, Boris Slutsky, Amit Mizrahi, Liang Feng, Vitaliy Lomakin, and Yeshaiahu Fainman, "Room Temperature Lasing from Subwavelength Metallo-Dielectric Lasers," Nature Photonics 4, 395-399 (2010).

Steve Zamek, Amit Mizrahi, Liang Feng, Aleksandar Simic, and Yeshaiahu Fainman, "Planar Dielectric Waveguide Cavity with Metallic Mirrors," Optics Letters 35, 598-600 (2010).

Amit Mizrahi, Vitaliy Lomakin, Boris Slutsky, Maziar P. Nezhad, Liang Feng and Yeshaiahu Fainman, "Low Threshold Gain Metal Coated Laser Nanoresonators," Optics Letters **33**, 1261-1263 (2008).

FIELDS OF STUDY

Major field: Electrical Engineering (Photonics)

     Studies in Photonics
     Professor Yeshaiahu Fainman
     Professor Vitaliy Lomkain

ABSTRACT OF THE DISSERTATION

Chip-Scale Plasmonic Resonant Nanostructures: Manipulation of Light from Nano to

Micro Scale

by

Liang Feng

Doctor of Philosophy in Electrical Engineering (Photonics)

University of California, San Diego, 2010

Professor Yeshaiahu Fainman, Chair
Professor Vitaliy Lomakin, Co-Chair

Nanophotonics is finding myriad applications in information technology, health care, lighting and sensing. Plasmonics, as one of the most rapidly growing fields in nanophotonics, has great potential to revolutionize many applications in nanophotonics, including bio-sensing, imaging, lighting, photolithography and magnetic recording. In this dissertation, we explore the electrodynamics of plasmonic fields on different structured metallic chips and demonstrate how to manipulate light from nano to micro scale on the structure plasmonic chips.

It is highly desired to excite and control propagation of surface plasmon polariton fields in a systematic fashion as it is possible with optical fields both in free space and dielectric waveguides. To accomplish this goal, we developed the design methodology compatible with the conventional Fourier optical devices, investigated on-chip plasmonic metamaterials with novel material response and functionalities, as well as constructed sophisticated chip-scale integration of different optical elements.

We begin by discussing the fundamentals of plasmonic fields and modal propagation properties. We next investigate a metallic metamaterial showing form-birefringence by engineering the inherent metal properties on nanoscale, and experimentally characterized their supported plasmonic index ellipsoids. We present novel experimental and analytic results of plasmonic nano metamaterials allowing excitation of plasmonic fields by transverse electric polarized incidence, complementing so far demonstrated transverse magnetic polarized excitation. We further construct a plasmonic photonic crystal to manipulate the propagating plasmonic field on a micro scale. On a lager sub-millimeter scale, we experimentally validated the feasibility of Fourier plasmonics, demonstrating possibilities of miniaturizing the conventional bulky optical devices on small plasmonic chips. We ultimately integrate various photonic components on different scales and provide an approach for efficiently using resonant plasmonic phenomena to achieve nanoscale optical field localization.

Chapter 1 Introduction

1.1 Motivation

Nanophotonics is finding myriad applications to improve information technology, health care, lighting and sensing [1-4]. Over the past decades, nanophotonics has been rapidly growing with the recent advancement of fabrication technology on micro and nano scales. The complexity of for the miniaturization of future systems will increasingly rely on optical interconnections, where the efficient on-chip manipulation of light on different scales is necessary.

Plasmonics [5], as one of the most important fields in nanophotonics, has great potential to revolutionize many applications in nanophotonics, including bio-sensing [6, 7], imaging [8-11], lighting [12-15], photolithography [16-18] and magnetic recording [19, 20]. Surface plasmon polaritons (SPPs) are formed due to strong interactions between electromagnetic fields and free electron oscillations on the metal-dielectric interfaces [5] and can be highly confined near the interfaces and intrinsically localized in a small volume on different structured metallic chips. This nanoscale plasmonic field confinement can significantly reduce average power requirements for nonlinear optical processes (such as surface enhanced Raman scattering [6]) and enable sub-diffraction limited imaging and waveguiding. More importantly, the intrinsic SPP field localization can help to beat the conventional diffraction limit, thereby showing a potential for full optical confinement on the nanoscale in all three dimensions beyond the diffraction limit of optical fields. Therefore, compact integration of optical devices is achievable on

plasmonic chips, which is expected to bridge the gap between nanophotonics and conventional electronics technologies. However, there are still a number of fundamental issues that need to be investigated for plasmonic optical elements to realize sophisticated on-chip light manipulation on different scales for future technologies.

To accomplish the practical functionalities for plasmonic optical elements, it is highly desirable to excite and control propagation of SPP fields in a systematic fashion as it is possible with optical fields both in free space and dielectric waveguides. It requires the design methodology available from the conventional Fourier optical devices, on-chip plasmonic metamaterial with novel material response and functionalities, as well as sophisticated chip-scale integration of different optical elements. This dissertation explores the electrodynamics of SPP fields on different structured metallic chips and demonstrates how to manipulate light from nano- to micro-scale on the structured plasmonic chips. The objective of this dissertation is to engineer metallic structures and plasmonic optical elements on the scale from nanometers to tens of microns. This work will first focus on (i) the development of metallic metamaterials that exhibit novel plasmonic properties and optical responses which reduce to (ii) wavelength scale plasmonic photonic crystals. Further increasing the scale leads to (iii) the demonstration of Fourier Plasmonics that realizes conventional Fourier optics to miniaturize bulky optical devices on a plasmonic chip, and finally (iv) describe a nanophotonic device that implements an on-chip deep sub-wavelength nanoscale optical field localization.

1.2 Dissertation organization

The dissertation is organized as follows. Chapter 2 reviews the basics of SPP propagation on the metal-dielectric interfaces. This includes an overview of the fundamental propagating SPP field distribution, propagation characteristics, as well as a summary of commonly employed methods for optical coupling to these modes. In addition to propagating SPPs, we discuss the localized surface plasmons (LSPs) and their associated resonant characteristics as well as potential applications.

Chapter 3 describes an approach on a deep subwavelength scale to manipulate the intrinsic properties of metals and therefore provide more freedom to design their supported SPPs. We report an artificial uniaxial birefringent metal that exhibits different dielectric polarizabilities along different optical axes as well as its supported optical anisotropy of SPP waves. This anisotropic birefringent plasmonic metamaterial establishes its optical plasmonic anisotropy as an SPP index ellipsoid can be observed. The generated plasmonic index ellipsoid that exists in reciprocal space has been directly mapped and characterized in our experiment.

Chapter 4 presents that a designer plasmonic metamaterial that is also engineered on a deep subwavelength scale in visible optical frequencies overcomes SPP's fundamental limitation of transverse magnetic (TM) polarized excitation, and allows transverse electric (TE) polarized incidence to be strongly coupled to surface plasmons. The experimental verification, which is consistent with the analytical and numerical models, demonstrates this extraordinary TE-plasmon coupling with efficiency close to 100% that is far from what is possible through naturally available materials.

Chapter 5 develops an approach to control SPP fields on the order of a wavelength. We designed and fabricated a dielectric plasmonic photonic crystal for manipulating SPP fields. The band structure of SPP fields inside the plasmonic photonic crystal has been calculated using the plane wave expansion method and validated by full wave numerical simulations. The fabricated device was characterized using our far-field SPP imaging technique. The transmittance of incident SPP waves is about 5% at 1520 nm (a designed bandgap frequency), confirming the designed band structure. The results show, both experimentally and theoretically, a complete two-dimensional bandgap for in-plane SPP waves. The SPP fields at frequencies within this specified $0.14\,\omega a/2\pi c$-wide bandgap frequency range are forbidden to propagate through the plasmonic photonic crystal.

Chapter 6 presents an in-plane Fresnel zone plate (FZP) for focusing SPP fields designed by Fourier plasmonics on the scale of tens of microns. The fabricated device consists of 400 nm tall by 5 nm wide amorphous Si-based SPP FZP on an Al film integrated with a pair of two-dimensional nanohole arrays for excitation of the incident and detection of the diffracted SPP fields. Diffracted SPP fields from each Fresnel zone constructively interfere at the expected focal point to produce focusing with 3-fold intensity enhancement. Temporal and spatial characteristics of the focused SPP fields are studied with time-resolved spatial-heterodyne imaging technique. Good agreement with average power measurements is demonstrated.

Chapter 7 demonstrates use of several plasmonic resonant phenomena combined with strong field localization to enhance efficiency of confining optical fields in a Si waveguide. Our approach utilizes a plasmonic resonant nano-focusing-antenna (RNFA),

that simultaneously supports several focusing mechanisms in a single nanostructure, integrated with a lossless Si waveguide utilized with silicon-on-insulator (SOI) technology, to achieve a sub-diffraction limited focusing with a nanoscale (deep subwavelength) spot size. The metallic RNFA effectively converts an incoming propagating waveguide mode to a localized resonant plasmon mode in an ultrasmall volume in all 3 dimensions. The near-field optical measurements of the fabricated RNFA using heterodyne near-field scanning optical microscope (H-NSOM) validate the theoretical predictions showing strong optical field localization.

Chapter 8 summarizes the major contributions of this work and discusses potential future research directions.

Chapter 2 Review of Surface Plasmon Polaritons

In this chapter, we first review the basic optical properties of metals. We then discuss the properties of propagating SPPs at a planar metal-dielectric interface by solving the Maxwell equations with the proper boundary conditions. With the understanding of basic properties of SPPs, we then summarize several approaches for excitation of SPP modes, including coupling by both electrons and electromagnetic fields. Among them, we will emphasize two techniques for coupling light to SPP modes: the Kretschmann-Raether configuration and grating coupling, which are mainly used later in this dissertation. We then discuss the optical properties of metallic nanoparticles as well as their associated localized plasmonic fields.

2.1 Optical properties of metals

The optical properties of metals are usually described by the Drude model that was first proposed by Paul Drude in 1900 [21]. The model, based on the kinetic gas theory, assumes the microscopic behavior of electrons in a metal can be treated classically with a sea of independent electrons bouncing off heavier and relatively stationary positive ions with a common relaxation time γ. The frequency dependent dielectric function ε can be expressed as:

$$\varepsilon(\omega) = \varepsilon_\infty - \frac{\omega_p^2}{\omega^2 - i\omega\gamma},$$
(2.1)

where ε_∞ includes the contribution of the bound electrons to the polarizability and ω_p is the so called plasma frequency.

With the plasma concept, the free electrons of metals can be viewed as moving in a positive charged background and the systems keep neutral macroscopically. Due to the movement of electrons and the interactions between different electrons, the system exhibits the fluctuation of the electron density microscopically. Because the interaction between electrons is Coulomb potential, the local electron density fluctuation can result in a long-range correlation of electrons in the entire system. Assume that every electron has a movement of x to the positive charged background, thereby resulting in an electric field:

$$E = 4\pi nex,$$ (2.2)

where n is the electron density. The recovery force on each electron is $-eE$ and the movement of electrons follows:

$$m*\ddot{x} = -4\pi ne^2 x,$$ (2.3)

where $m*$ replaces the free electron mass m_e and it is obtained by approximating the real dispersion relation of the metal's band structure in the limit of small k. All the electrons are therefore resonantly oscillating with the same frequency, the plasma frequency ω_p,

$$\omega_p^2 = \frac{4\pi ne^2}{m*}.$$ (2.4)

At the plasma frequency, all the electrons oscillate resonantly and this collective electron density resonance is called "volume plasmons". An important extension of the plasmon physics has been accomplished by the concept of "surface plasmons", when the infinite metal is terminated by a surface. We explore the properties of these surface plasmons on metal-dielectric interfaces in the next section.

2.2 Optical properties of SPPs on metal-dielectric interfaces

The basics of SPPs propagation on a planar metallic surface are summarized by Raether [5]. The interface between the metal and the dielectric medium lies in the *x-y* plane as shown in Fig. 2-1. We assume SPPs propagation in the *x* direction with the electromagnetic fields exponentially decaying into the ± *z* directions.
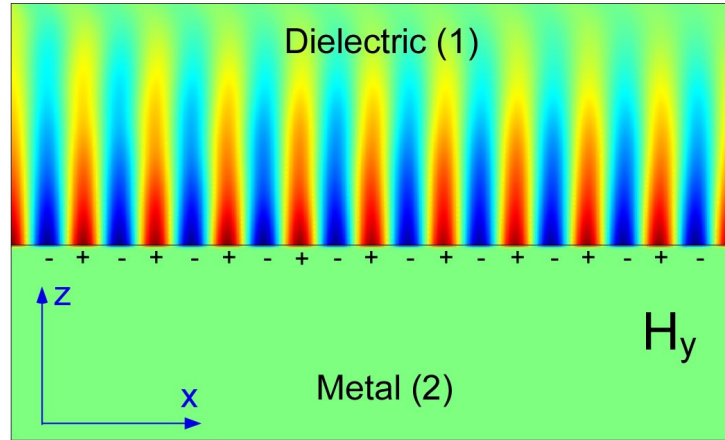
Fig. 2-1. The component H_y of the SPP mode at a smooth metal-dielectric interface. The electromagnetic eigen modes are TM polarized, and the fields are maximal at the interface ($z = 0$) and decay exponentially into both metals and dielectrics.

The fields in two infinite half spaces can be described by the following TM wave:

$$
\begin{aligned}
\mathrm{E}_j &= \left(E_x,\ 0,\ E_{z,j} \right) \exp\left(i \left(k_x x + k_{z,j} z - \omega t \right) \right) \\
\mathrm{H}_j &= \left(0,\ H_y,\ 0 \right) \exp\left(i \left(k_x x + k_{z,j} z - \omega t \right) \right)
\end{aligned}
, \tag{2.5}
$$

where $j = 1,2$ represents the dielectric medium or the metal, respectively. The fields need to match at the interface ($z = 0$). Hence, following Maxwell's equations and continuities at the boundary, we can have the relationship of fields at the boundary:

$$
D_0 = \frac{k_{z1}}{\varepsilon_1} + \frac{k_{z2}}{\varepsilon_2} = 0. \tag{2.6}
$$

Together with the relationship of fields in two different spaces:

$$k_{z,j} = \left[\varepsilon_j \left(\frac{\omega}{c} \right)^2 - k_x^2 \right]^{1/2}, \tag{2.7}$$

the wave vector k_x is continuous through the interface and its dispersion relation can be expressed as:

$$k_x = \frac{\omega}{c} \left(\frac{\varepsilon_1 \varepsilon_2}{\varepsilon_1 + \varepsilon_2} \right)^{1/2}. \tag{2.8}$$
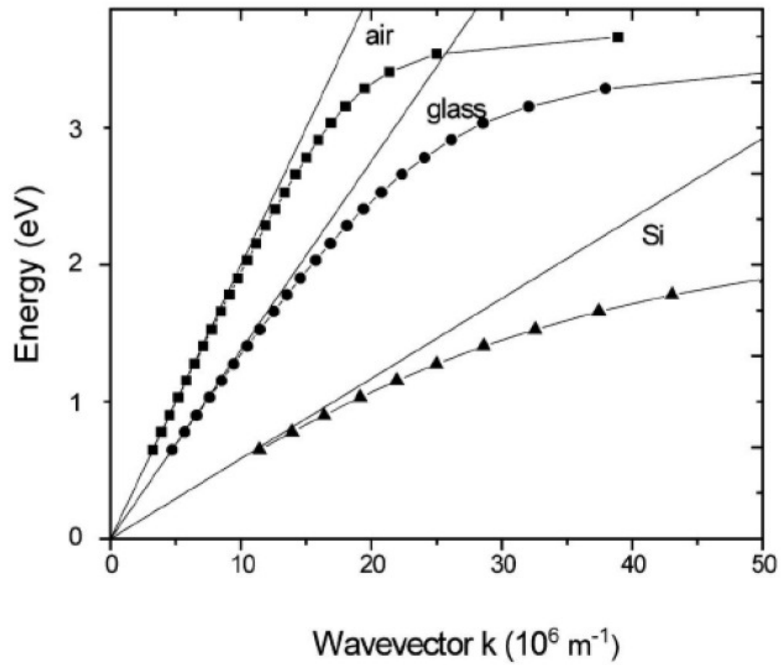
Fig. 2-2. Dispersion for SPPs on a smooth Ag film with different surrounding dielectrics.

This dispersion relation $\omega(k)$, see in Fig. 2-2, approaches the light line $\sqrt{\varepsilon_1}\,\omega/c$ at small k_x, but remains larger than $\sqrt{\varepsilon_1}\,\omega/c$, so that SPPs has a longer wav vector than the optical wares with the same energy $\hbar\omega$: it is a non-radiative surface wave propagating along the metal surface. The value of ω approaches

$$\omega_{spp} = \left(\frac{\omega_p}{1 + \varepsilon_1} \right)^{1/2}. \tag{2.9}$$

If assuming besides a real ω and ε_1 that region 2 has a complex dielectric constant ($\varepsilon_2 = \varepsilon_2' + i\varepsilon_2''$), we obtain a complex $k_x = k_x' + ik_x''$ from Eq. 2.8:

$$k_x' = \frac{\omega}{c}\left(\frac{\varepsilon_1 \varepsilon_2'}{\varepsilon_1 + \varepsilon_2'}\right)^{1/2} \tag{2.10}$$

$$k_x'' = \frac{\omega}{c}\left(\frac{\varepsilon_1 \varepsilon_2'}{\varepsilon_1 + \varepsilon_2'}\right)^{3/2} \frac{\varepsilon_2''}{2(\varepsilon_2')^2}. \tag{2.11}$$

The imaginary part of k_x, k_x'' is responsible for the propagation loss of SPPs along the interface, with a characteristic propagation length

$$L_{spp} = \frac{1}{2k_x''} = \frac{1}{k_0}\left(\frac{\varepsilon_1 + \varepsilon_2'}{\varepsilon_1 \varepsilon_2'}\right)^{3/2} \frac{(\varepsilon_2')^2}{\varepsilon_2''}. \tag{2.12}$$

This results from the non-zero imaginary part of the metal dielectric constant. It is highly desired to choose a metal with a high plasmonic resonance to increase the SPPs propagation length in the metal-dielectric interface.

2.3 Excitations of SPP waves

Electrons penetrating metals transfer momentum $\hbar q$ and energy ΔE_0 to the electrons of metals. The projection of q upon the surface of the metal, k_x, determines the wave vector of the excited SPP waves. Together with the dispersion relation, the energy loss from the scattered electrons corresponding to the energy of excited SPP waves $\Delta E = \hbar\omega$ can be detected. Therefore, fast electrons used to be a good tool to study the dispersion relation of SPPs [22, 23]. However, it is not convenient to reach the region of

small k_x with electrons, either fast or slow, since the aperture of the electron beam can not be sufficiently reduced.

More popular approaches to excite SPP waves are to directly couple light into SPPs. In this work, we are exclusively interested in excitation of SPPs by photons. This process meets the difficulty that the dispersion relation lies right from the light line, requiring larger wave vector for SPPs than the photons exciting them. The most commonly employed methods of coupling to SPPs include evanescent field coupling methods via a prism in the Kretschmann-Raether [24] and Otto [25] configurations and with a near-field scanning optical microscope (NSOM) tip [26]. Simply random surface roughness can also provide the momentum mismatch to excite SPPs [27] but grating coupling can be accomplished with a better coupling efficiency if the phase matching condition is satisfied for SPPs [28]. Among them, we will mainly introduce two schemes: the Kretschmann-Raether configuration using total internal reflection coupling and grating coupling.
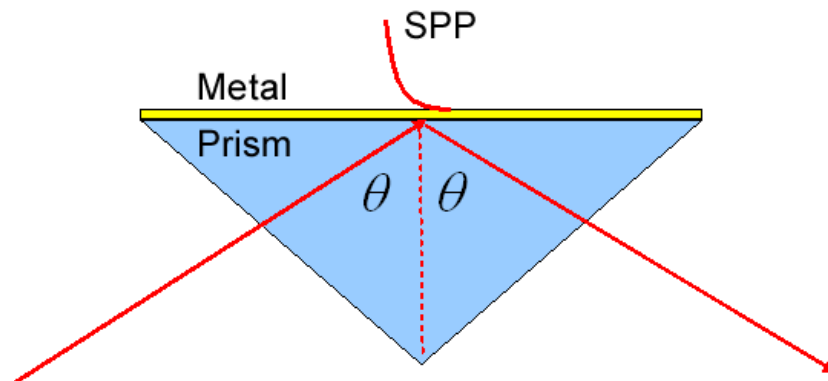
Fig. 2-3. Kretschmann-Raether configuration for coupling light to SPPs.

In the Kretschmann-Raether configuration as shown in Fig. 2-3, light is incident to the metal from a prism. When the light is reflected at the metal-prism boundary with

the prism dielectric constant $\varepsilon_3 > \varepsilon_1$, the projection of the wave vector on the surface is

$k_x = \sqrt{\varepsilon_3} k_0 \sin\theta$, where θ is the incidence angle. While this in-plane momentum is not

sufficient to excite SPPs on the interface of the metal and the prism, if the metallic film is

thin enough, electromagnetic field can evanescently couple to the surface mode on the

other metal interface (e.g. metal-air) and excite SPPs at the incidence angle θ_0 when the

phase matching condition is satisfied:

$$k_x = \sqrt{\varepsilon_3} k_0 \sin\theta = k_0 \left(\frac{\varepsilon_1 \varepsilon_2}{\varepsilon_1 + \varepsilon_2} \right) = k_{spp} . \tag{2.13}$$

This type of SPP excitation can be realized with nearly 100% coupling efficiency. As a

consequence, the minimal in the reflection spectrum corresponds to the maximum

excitation of SPPs [29].
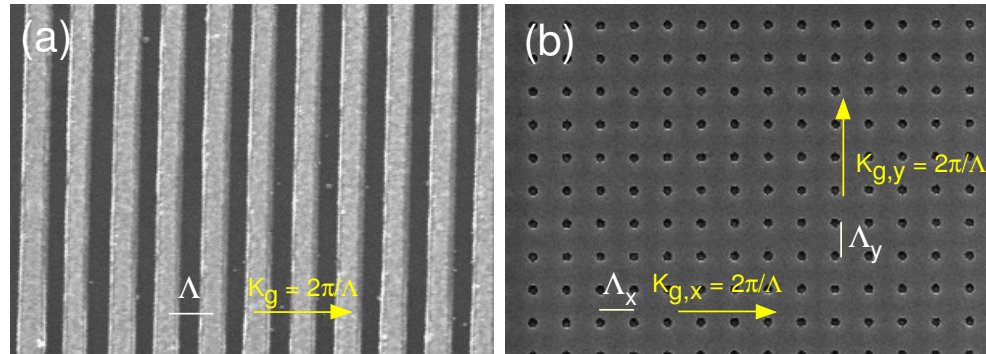
Fig. 2-4. SEM images of (a) 1D metallic grating and (b) 2D metallic nanohole array with providing additional grating vectors for coupling light to SPP waves.

When light illuminates a metallic grating with a period of Λ as shown in Fig. 2-4(a), the wave vector of the diffracted wave on the grating is modulated by the grating

vectors as

$$k_x = k_0 \sin\theta_0 \pm m K_g . \tag{2.14}$$

Integer number of the grating vectors $K_g = 2\pi/\Lambda$ are added or subtracted from the projection of the incident optical filed wave vector $k_0 \sin\theta_0$ on the grating, according to the diffraction order m. Under the appropriate conditions that phase matching by mK_g can satisfy the SPP dispersion relation ($k_x = k_{spp}$), the incident optical field can thus be converted to SPP waves on the metallic grating.

The concept of grating coupling of SPP waves has been further extended with a two-dimensional (2D) metallic nanohole array [30], as shown in Fig. 2-4(b), in order to have more freedom in manipulation of SPPs excitation. The incident optical field excites a SPP wave on the metallic nanohole array when the sum of its in-plane component of the wavevector and a combination of reciprocal lattice vectors satisfies the following phase matching condition:

$$k_{spp} = k_{\parallel} \pm mK_{g,x} \pm nK_{g,y}, \tag{2.15}$$

where k_{spp} is the wave vector of the SPP wave, $K_{g,x}$ and $K_{g,y}$ are the grating vectors in the x and y directions, respectively, m and n are integers of diffraction orders of the excited SPP, and $k_{\parallel}$ is the in-plane component of the incident wave vector and can be expressed as:

$$k_{\parallel} = k_x + k_y = k_0 \left(\hat{x}\sin\theta\cos\phi + \hat{y}\sin\theta\cos\phi \right) \tag{2.16}$$

for the square lattice. SPP waves excitation and propagation in such metallic nanohole arrays have been successfully imaged and elaborately studied with a far-field imaging setup [31, 32] that we will apply to the work in Chapter 5 and Chapter 6. The excitation of SPP waves on the metallic nanohole array can significantly enhance the optical

transmission through these subwavelength apertures and as a consequence, extraordinary optical transmission associated with SPPs and other resonant phenomena has been an important subject with extensive recent investigations [30, 33-40].

2.4 Localized surface plasmons

Localized surface plasmons (LSPs) are collective electron charge oscillations in metallic nanoparticles when excited by light. Since the resonance here is limited to the nanoparticles, it is often called "localized" [41, 42] as comparing to propagating SPPs we discussed above. In the case of a nano-sphere, the corresponding condition for LSPs is given by [43]

$$\varepsilon_m(\omega) = -\varepsilon_0 \frac{l+1}{l}, \quad l = 1, 2, 3... \tag{2.17}$$

where the lowest mode $l = 1$ can be calculated from $\varepsilon_m(\omega) = -2\varepsilon_0$. These modes are radiative and the curved surface couples the modes with photons, so they are damped in addition to the internal damping by light emission.

This relation can also be obtained from calculating the polarization of a sphere in a uniform exterior electric field E_0

$$P(\omega) = \frac{3}{4\pi} \frac{\varepsilon_m(\omega) - \varepsilon_0}{\varepsilon_m(\omega) + 2\varepsilon_0} E_0. \tag{2.18}$$

This equation is only valid in quasi-static electric regime as long as the sphere is much smaller than the free space wavelength. The field at the surface of the metallic sphere ($\varepsilon_0 = 1$) is

$$E_s = 2 \frac{\varepsilon_m - 1}{\varepsilon_m + 1} E_0 + E_0 = \frac{3\varepsilon_m}{\varepsilon_m + 2} E_0, \tag{2.19}$$

which has a maximum for $\varepsilon_m{}' = -2$ and gives an enhancement of

$$T = \left(\frac{E_s}{E_0}\right)^2 = \left(\frac{3\varepsilon_m{}'}{\varepsilon_m{}''}\right)^2 .$$
(2.20)

This shows that the electric field on the metallic nano-sphere surface is typically a few orders higher than the incident optical field. Due to this significant field enhancement, a number of efforts have been carried on to apply LSPs to improve myriad optical nonlinear activities, especially in surface enhanced Raman scattering [44], enhanced fluorescence [45], etc. Different metallic geometries, such as metallic ellipsoids [46, 47], have been investigated to further improve the field enhancement and localization. It has also been suggested that electromagnetic energy can be guided below the diffraction limit through the near-field LSP coupling using an array of closely packed metallic nanoparticles [48-50]. The integration of LSPs with propagating SPP waves gives an additional knob to better control and excite LSPs on local metallic nanostructures [51].

Besides the dipolar electric LSPs we discussed above, a series of more complicated geometries, such as split ring resonators [52-55], metallic pairs [56, 57], have been intensively studied to demonstrate the localized magnetic resonance for realizing magnetic responses and negative permeability in optical frequencies. The simultaneous realization of both negative permittivity and negative permeability leads to negative index of refraction, bending the light in a wrong direction [58-60]. Imaging resolution improvement with negative refraction has been experimentally validated as shown in recently developed superlenses [8-10, 61].

Chapter 3 Form Birefringent Metal and Its Supported Plasmonic Anisotropy

3.1 Introduction

Optical anisotropy refers to optical materials which possess polarizability that depends on the direction of propagation of electromagnetic fields. This phenomenon originates from atomic scale dipole moments that vary in space depending on the crystal lattice structure. The susceptibility and the corresponding polarizability of such media will vary in space depending on the propagation direction and the state of polarization of the optical fields propagating in such media. Consequently, such crystals possess indices of refraction that depend on the crystallographic lattice structure and in most general case are described in reciprocal space by an index ellipsoid in three dimensions [62, 63]. Optical anisotropy in dielectrics has been used to create various devices which found applications in displays, communication, storage, and computing. More recently, space-variant polarizability of isotropic dielectrics has been achieved by creating a deep sub-wavelength structure composed of two or more materials [64-67] such that in electrostatic field approximation it acts similarly to that of an anisotropic crystal, where the sub-wavelength scale geometry can have average polarizability varying in three dimensions of the medium. These structures called "form birefringence" have been also used for various applications to manipulate the polarization state of the fields in forms that are not possible with natural birefringent crystalline dielectrics [68, 69].

Recently, plasmonic phenomena that uses interaction of light and surface electrons on a metal-dielectric boundary has attracted attention due to its ability to strongly confine light near the interface and intrinsically localize light in small volumes [5]. The utilization of SPP can help to create optical field localization devices, enable novel functionalities on a nanometer scale. These devices, although lossy due to their physical origin, are making an impact on such uniquely suitable applications as nano-imaging [8-10], label-free biochemical sensing [6, 7], nano-photolithography [16-18], and data storage [19, 20]. Note, that although the reported applications use isotropic plasmonic properties of metals, some applications [70] would be enabled by plasmonic anisotropy. However, in practice, it is difficult to realize optical plasmonic anisotropy because the optical properties of metals are isotropic. Here, we report a uniaxial form birefringent metal that exhibits different dielectric polarizabilities along different optical axes as well as its supported optical anisotropy of SPP waves. The generated plasmonic index ellipsoid that exists in reciprocal space has been directly mapped and characterized in our experiment. The discovery of this anisotropic plasmonic metamaterial further completes analogy between artificial plasmonic metamaterials and conventional optical crystals, thereby providing new opportunities to miniaturize myriad existing optical devices on-a-chip with plasmonics into nanometers scale

3.2 Form birefringent metal

A new type of artificial metamaterial consisting of metallic wires in a host dielectric medium has been proposed and analyzed using the effective medium theory [71]. The reported metal-dielectric composite acts as a slab with novel hyperbolic

dispersion properties that have been used to manipulate the propagating optical fields inside the slab, showing negative refraction [72, 73]. In this chapter, we propose and experimentally demonstrate for the first time a metal-dielectric composite metamaterial, in contrast to Refs. [72, 73], composed of dielectrics in a host metal that acts as an anisotropic uniaxial birefringent metal in the long wavelength approximation regime, supporting propagating SPP waves on the surface. Our metal-dielectric composite transfers its material birefringence to the SPP's. We construct the effective index ellipsoid of such a metal-dielectric composite and show numerically and experimentally the corresponding SPP modes using the reciprocal space representations.
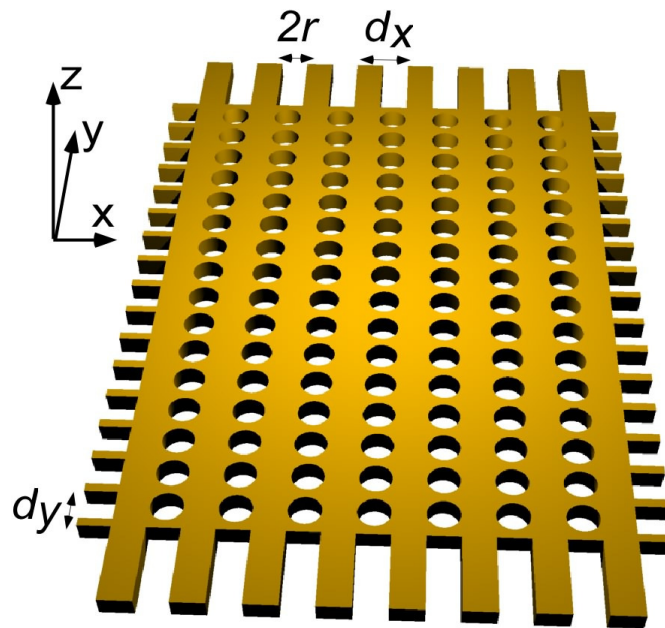
Fig. 3-1. Form birefringent metal acting as an anisotropic plasmonic metamaterial: Schematic of a 55 nm-thick Au from the birefringent metal with the designed parameters: d_x = 140 nm, d_y = 140 nm and r = 35 nm.

The form birefringent metal acting as an anisotropic plasmonic metamaterial, schematically depicted in Fig. 3-1, is a two-dimensional (2-D) array of air nanoholes in a thin metal film implementing a deep subwavelength periodic structure with periods

differing in x and y directions. The effective dielectric constant tensor of this metamaterial can be described as:

$$\varepsilon_{eff} = \begin{pmatrix} \varepsilon_x & 0 & 0 \\ 0 & \varepsilon_y & 0 \\ 0 & 0 & \varepsilon_z \end{pmatrix}, \tag{3.1}$$

and using the effective medium theory the three diagonal elements are approximately expressed by [71]

$$\varepsilon_x = \varepsilon_m \left(1 - \frac{\pi r^2}{2d_y r} \right) + \varepsilon_0 \frac{\pi r^2}{2d_y r}$$

$$\varepsilon_y = \varepsilon_m \left(1 - \frac{\pi r^2}{2d_x r} \right) + \varepsilon_0 \frac{\pi r^2}{2d_x r} \tag{3.2}$$

$$\varepsilon_z = \varepsilon_m \left(1 - \frac{\pi r^2}{d_x d_y} \right) + \varepsilon_0 \frac{\pi r^2}{d_x d_y},$$

where ε_m and ε_0 are the dielectric constants of metal (e.g., Au [74]) and dielectric medium in the nanoholes (e.g., air), respectively, r is the radius of nanoholes, and d_x and d_y are the periods of the deep subwavelength structure in the x and y directions, respectively. Since all three parameters in Eq. (3.2) are negative, the constructed metamaterial can be considered as an anisotropic metal. Therefore, it is evident that the different effective dielectric constants will inevitably result in different SPP eigen modes with their corresponding dispersion relations along the x and the y axes, thus creating optical anisotropy for SPP fields.

3.3 Experiment fabrication and measurement setup

To validate our proposed anisotropic plasmonic metal-dielectric metamaterial, we use focused-ion-beam (FIB) milling to fabricate fine deep subwavelength features shown in Fig. 3-1 using an Au film on a glass substrate. The SEM micrograph of the fabricated structure is shown in Fig. 3-2. The excited SPP modes in the fabricated metamaterial are characterized in reciprocal space by analyzing reflection images (see Fig. 3-3) obtained from the glass substrate side of the samples inserted in an oil immersion microscope objective (MO) with high numerical aperture (NA=1.4).
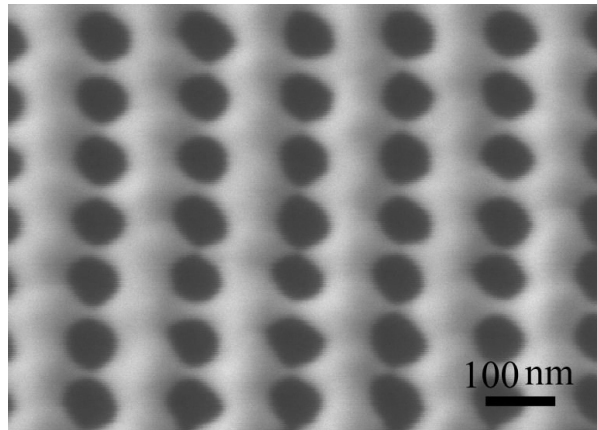
Fig. 3-2. SEM micrograph of the fabricated structure using FIB milling.

A converging unpolarized spherical wave is used as an illumination function to code a wide-band angular momentum of the illumination function to a constant radial position within the illumination circle. Lens 1 and the microscope objective are used to construct a typical 4-f imaging system. Lens 2 is inserted against the image plane to perform a Fourier transformation of the information in the image plane (the coherence length for the 10 nm bandpass filter with the center wavelength of 540 nm is 29.16 μm and the maximum optical path difference in our setup is about 11.2 μm). The CCD

camera is located at the focal plane of lens 2 so that it can directly capture the corresponding Fourier transform, which represents the SPP's index ellipsoid in the k space. Some of these spatial frequencies satisfy the phase matching condition and thus excite SPPs.
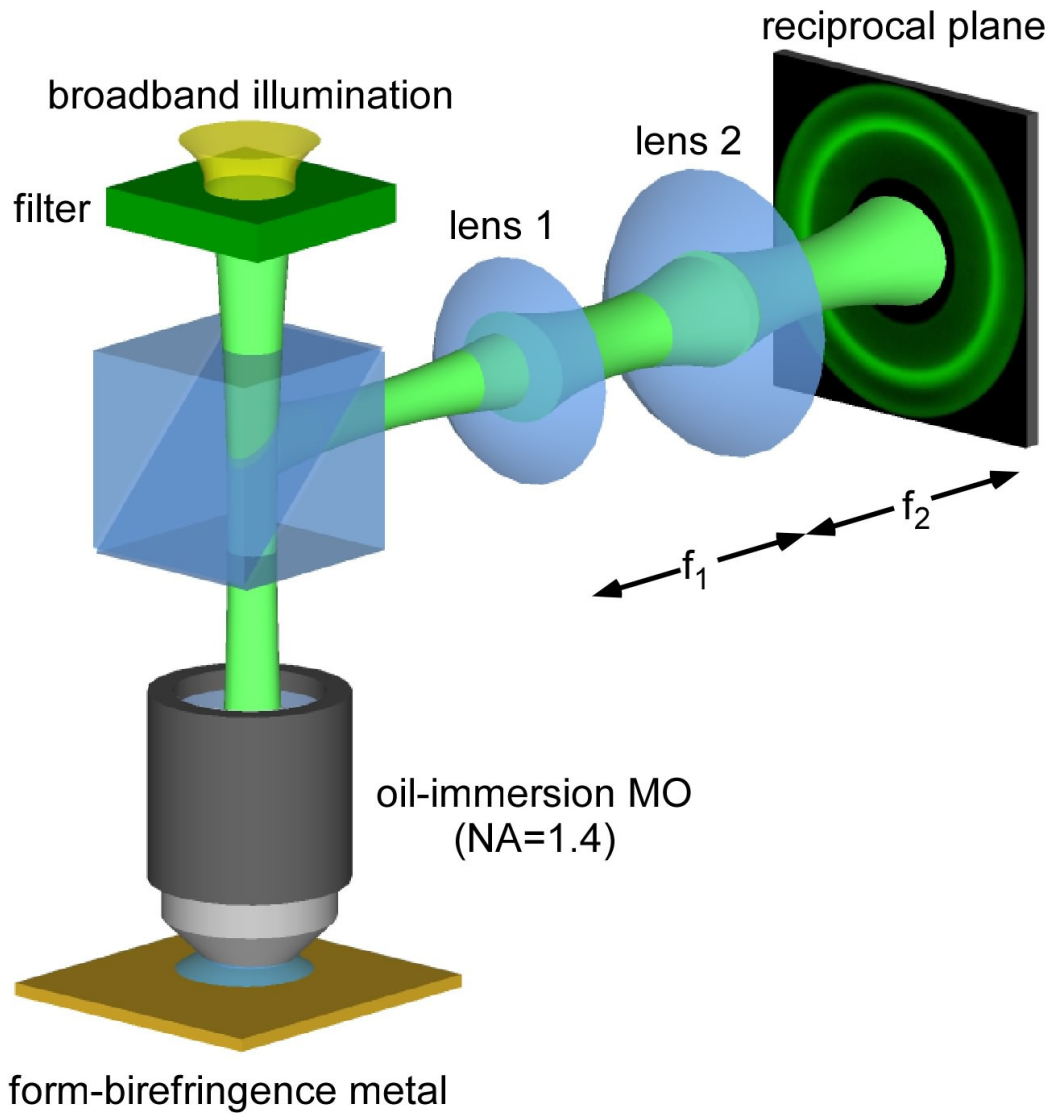
Fig. 3-3. Measurement setup to directly image SPP's index ellipsoid in reciprocal space in the far field, consists of a broadband source, an oil immersion microscope objective with NA=1.4, two lenses and a CCD camera.

3.4 Anisotropic surface plasmons

Fig. 3-4 shows the numerically simulated and experimentally measured index ellipsoids of SPPs on the artificial form birefringent metal in reciprocal space at the wavelength around 540 nm. They are in a good agreement, with different effective SPP indices along different azimuthal directions, exhibiting anisotropic SPPs excitation.
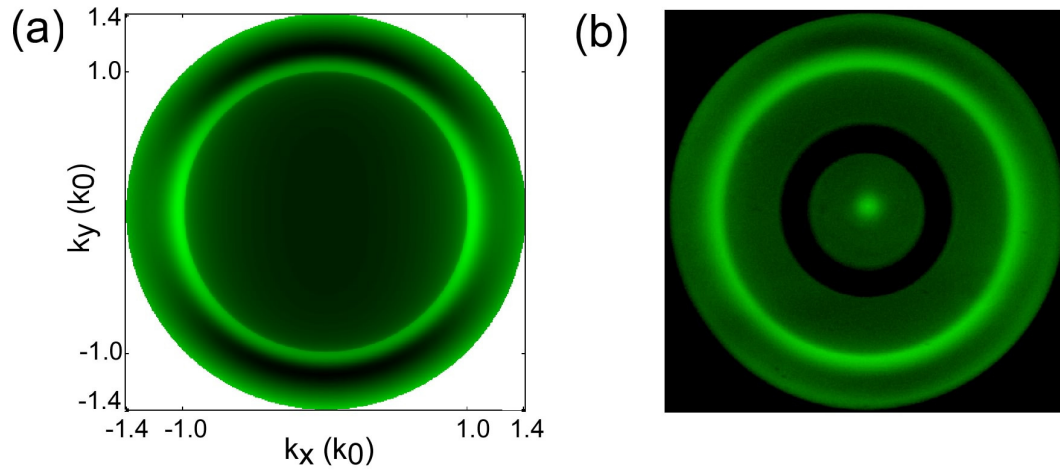
Fig. 3-4. Characterization of SPP's index ellipsoid at the center wavelength of 540 nm. (a) Simulated SPP's index ellipsoid in a representation of reflected power distribution in reciprocal space. (b) Experimental imaging of reflection from the metamaterial in reciprocal space.

Since the image on the CCD is created by the reflected field (where the SPP on metal-air interface are also excited for rays with angular spectrum satisfying the SPP phase matching condition, the excited SPP index ellipsoid corresponds to a dip (i. e., loss) where the generated SPP undergoes material loss and consequently gets dissipated (similar to the Kretschmann-Raether configuration that uses prisms to excite SPPs [24]). The size of the obtained image is limited by the NA of our MO that corresponds to a free space wavevector of 1.4 k_0. Note that the central dark ring in Fig. 3-4(b) (i.e., image of the phase ring inside the phase contrast MO) obscures some information but the information of interest here occurs at larger wavevectors. The bright circle represents the

boundary of the illumination at the angle corresponding to total internal reflection (TIR) when the transverse component of the illumination wavevector is k_0. Outside this TIR circle, an elliptical dark ring caused by excitation of SPPs manifests the optical plasmonic anisotropy of the excited SPP waves. From this index ellipsoid, we can also retrieve experimentally the effective wavevectors of SPP modes propagating along x and y optical axes as well as other azimuthal angles.
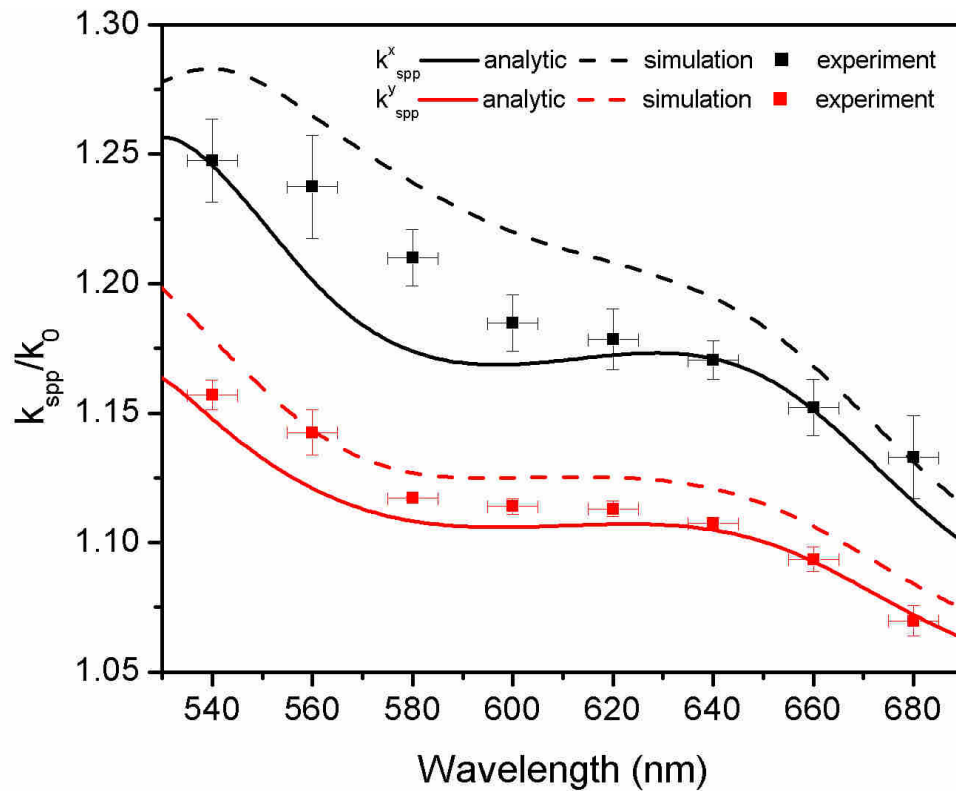
Fig. 3-5. Anisotropic SPP dispersion relations. Black and red symbols represent SPP's wavevectors along the *x* and *y* directions, respectively. Solid curve, dashed curve and square dot correspond to the data retrieved from analytical calculations according to Eqs. (3.1)-(3.3), numerical simulations and experimental measurements, respectively. For experimental data, the error-bar in wavelengths indicates the bandwidth (10 nm) of the bandpass filters used in the experimental measurement.

With considering the boundary continuity, the eigen vectors of SPPs along x and y axes yield

$$k_{spp}^{x,y} = k_0 \sqrt{\frac{\varepsilon_0 \varepsilon_z \left(\varepsilon_{x,y} - \varepsilon_0 \right)}{\varepsilon_{x,y} \varepsilon_z - \varepsilon_0 \varepsilon_0}} \ , \qquad\qquad (3\text{-}3)$$

where k_0 represents the wavevector of light in free space. The experimentally measured wavevectors from Fig. 3-4(b) are integrated into Fig. 3-5 for comparison with the analytical calculations using Eq. (3.3) and numerical simulations in which the wavevectors of SPPs is determined as the positions of dips in the simulated reflection spectra. The index ellipsoid and SPP's dispersion relations of wavevectors are measured as a function of optical wavelength by analyzing images obtained using a series of 10 nm bandpass interference filters in the spectral range of interest, i.e., from 540 nm to 680 nm. The plasmonic anisotropy in the range of interest attributes to the effective dipole moments engineered in an "artificial-atomic" scale with deep subwavelength features that vary in space depending on the crystal lattice of our form birefringent metal. The effective SPP indices in different directions vary since the plasmonic field interactions between unit cells strongly change with different duty cycles and dipole orientations, and thus manifest different averaged plasmonic E-fields in both individual unit cells and holes.

Polarized illumination was used to extract more detailed features and properties of the excited SPP modes on our form birefringent metal. Depending on the state of polarization of the illuminating field, only a fraction of SPP modes on the index ellipsoid will be excited. Both measured and simulated results are consistent with the results shown in Fig. 3-4 obtained with unpolarized illumination. When the polarization of the illumination field is along one of the optic axes (see Figs. 3-6(a), 3-6(b), 3-6(d) and 3-6(e)), a symmetric SPP modes distribution with respect to the direction of the polarization is observed. Note, that the SPP wavevector propagating along the x direction has a

relatively larger wavevector but a smaller Quality factor with a wider spatial frequency bandwidth. When the illumination field is polarized at 45° with respect to the optic axes, the SPP modes distribution is clearly asymmetric along the x and y directions, suggesting plasmonic anisotropy. Data on SPP modes wavevectors extracted from Figs 3-6(c) and 3-6(f) are found in good agreement with the results obtained with unpolarized illumination (Fig. 3-4) and other polarizations in Fig. 3-6.
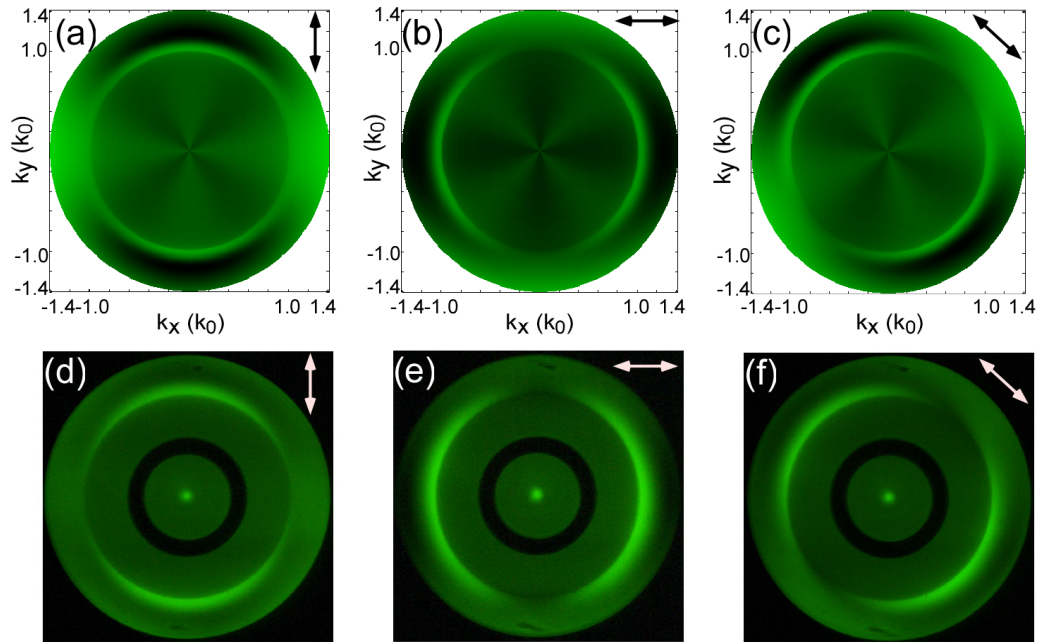
Fig. 3-6. Simulated and measured SPP index ellipsoids with different polarization orientations. (a)-(c) Simulated reflection map in reciprocal space. (d)-(f) Experimental imaging of reflection in reciprocal space. The polarization states in ((a), (d)), ((b), (e)) and ((c), (f)) are oriented along the *y*, *x* and at $45° -$ axis, respectively.

3.5 Summary

Analog to optical birefringent crystals in nature, an artificial "form birefringence" metal has been constructed and shown to demonstrate different polarizabilities along different optical axes. This material anisotropy leads to optical plasmonic anisotropy of excited SPP modes. This novel optical plasmonic anisotropy is investigated using

analytic calculations, numerical simulations and experimental characterizations. Plasmonic index ellipsoid is observed and mapped directly in reciprocal space, demonstrating anisotropic dependence on the polarization state of the fields. This optical plasmonic anisotropy further completes the analogy between plasmonic metamaterials and conventional optical crystals, enabling construction of plasmonic optical devices for applications that rely on chip-scale nanoscale field localization.

It is worth noting that the concept of "form birefringence" metal is not limited within the specific case shown above. The extension of this work to three dimensions also promises novel physics and applications. The 1D metamaterial is like the metallic wire grid polarizer that only acts as a metal when the state of the polarization is collinear with the axis of the wires. Therefore SPP index ellipsoid in reciprocal space only exists in a finite azimuthal angular regime centered symmetrically along wires. The 3D case can be designed more complicated to adapt more complex Bravais crystal lattices and thus realize a bi or multi-axial anisotropic metal that can support different SPP index ellipsoids on different cross-sections. The effective parameters of these form birefringent metals are decided by not only the designed geometries but also the index of dielectrics (e.g. air holes in this work). By filling high-index dielectrics in form birefringent metals, the effective plasma frequency of metals can be manipulated lower to the visible regime. Hence myriad important SPP phenomena currently demonstrated only in the UV regime such as superlensing [8-10] can be expected to construct in a much wider visible range with the emergence of "form-birefringence" metals. The effective plasma frequency of "form-birefringence" metals can be further actively controlled if the index of filled dielectrics is tunable. Therefore, "form-birefringence" metals provide more flexibility in

engineering inherent metal properties for complex homogeneous and inhomogeneous plasmonic devices that highly demand a wide-range adiabatic change of metal's dielectric constant [75] and SPP's index in optical circuit design.

3.6 Acknowledgements

Chapter 4 Metamaterial for Extraordinary Polarization Conversion in Plasmonic Excitation

4.1 Introduction

Due to the intrinsic transverse magnetic nature of plasmonic fields, however, SPPs efficient excitation is strongly constrained to TM polarized incidence, so that for unpolarized light, 50% of the energy that is TE polarized can not be utilized. Designer plasmons, also called *spoof* plasmons, refer to surface-plasmon-like waves on textured metal surfaces, which can be supported in periodic structures that may be made of perfect conductors [76-82]. Designer plasmons rely on evanescent or propagating modes inside the textured surface, with significant property variations for the two cases [76, 77]. The latter offers particular flexibility and can lead to surface modes with a very large wave vector. The existence of such plasmons can be attributed to the fact that the textured surface can be viewed as imposing an effective surface impedance, which can be artificially engineered by the structure geometrical parameters, such as the periodicity, duty cycle, and thickness of the metallic features. In the terahertz and microwave regimes, designer plasmonic metamaterials have been constructed to realize wave guidance and focusing [80, 81], as well as to engineer the slow wave characteristics of the guided microwave [82]. However, similarly to natural SPPs on metallic surfaces in the optical regime, such designer plasmons are also intrinsically TM polarized, and only the corresponding TM excitation has been demonstrated so far.

Textured metallic surfaces with designer plasmons in the optical regime have a high potential to result in a number of unique phenomena due to possible interplay

between the plasmonic properties of metals and properties derived from structural features of the textured surface. The complexity of the resulting electromagnetic phenomena may provide great freedom to tailor SPP propagation as well as design a TE-driven SPP, complementing the so far demonstrated TM-polarized excitation. In this chapter, we present, for the first time, an optical designer plasmonic metamaterial, which combines plasmonic properties of metals in optics and properties of designer textured surfaces typically observed for microwave structures. Such designer plasmonic metamaterial is engineered on a deep subwavelength scale in visible optical frequencies to overcome this fundamental limitation, and allows transverse electric (TE) polarized incidence to be strongly coupled to surface plasmons. The experimental verification, which is consistent with the analytical and numerical models, demonstrates this extraordinary TE to plasmon polarization conversion with efficiency close to 100%, far from what is possible through naturally available materials. This counterintuitive discovery will help to efficiently utilize the energy fallen into TE polarization and drastically increase overall excitation efficiency of future plasmonic devices.

4.2 Optical designer plasmonic metamaterial

The presented designer plasmonic metamaterial consists of Au stripes periodically arranged on a deep subwavelength scale, as shown in Fig. 4-1. So far similar metamaterials were analyzed only in two-dimensional (2D) configurations, and for the terahertz regime [77, 80, 82]. In contrast, in this study we operate in the optical regime, and consider an incident wave with a nonzero azimuth and elevation angles, requiring a fully three-dimensional (3D) analysis and physical understanding. The domain between

the top and bottom faces of the metamaterial acts as an array of metal-insulator-metal (MIM) plasmonic transmission lines [83], supporting plasmonic Bloch modes guided in the vertical direction. Because of the 3D nature of the problem, the modes are hybrid, consisting of both TM and TE polarized components. A combination of the modes guided in the upward and downward directions is required to satisfy the boundary conditions on the top and bottom faces of the metamaterials. Due to the extremely thin width of metallic stripes that is on the order of the skin depth, plasmonic modes in different MIM transmission lines are not independent and the introduced periodic potential makes a collectively oscillating plasmonic Bloch mode in the periodic array of transmission lines. In particular, the hybrid nature of the supported Bloch mode can provide mode overlap and bridge TE incidence and excited SP waves, thereby creating enhanced TE to plasmon coupling in the designer plasmonic metamaterial.
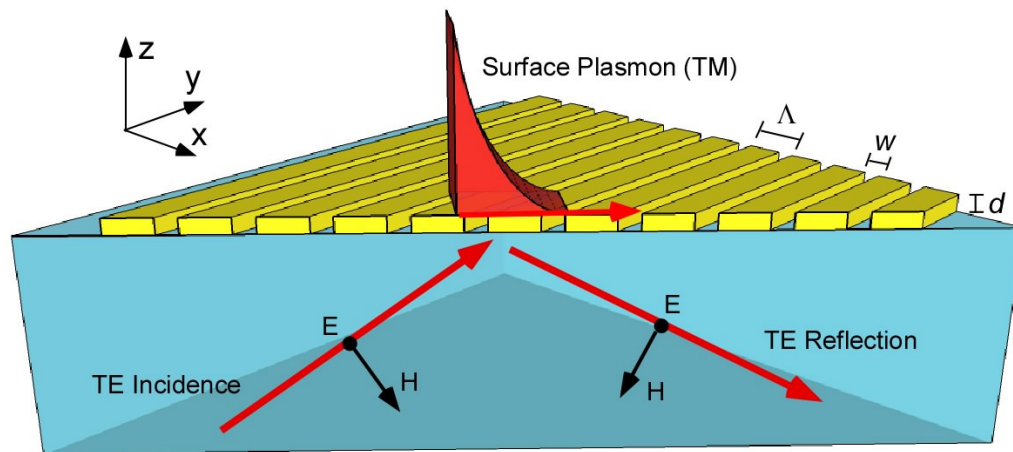
Fig. 4-1. Optical designer plasmonic metamaterial: Schematic of enhanced TE to plasmon coupling with the designer plasmonic metamaterial. TE-polarized plane wave incidents from a glass substrate ($n = 1.5$) with the incident plane as the diagonal cross-section of the metamaterial slab and excites SPPs at the air/metamaterial interface.
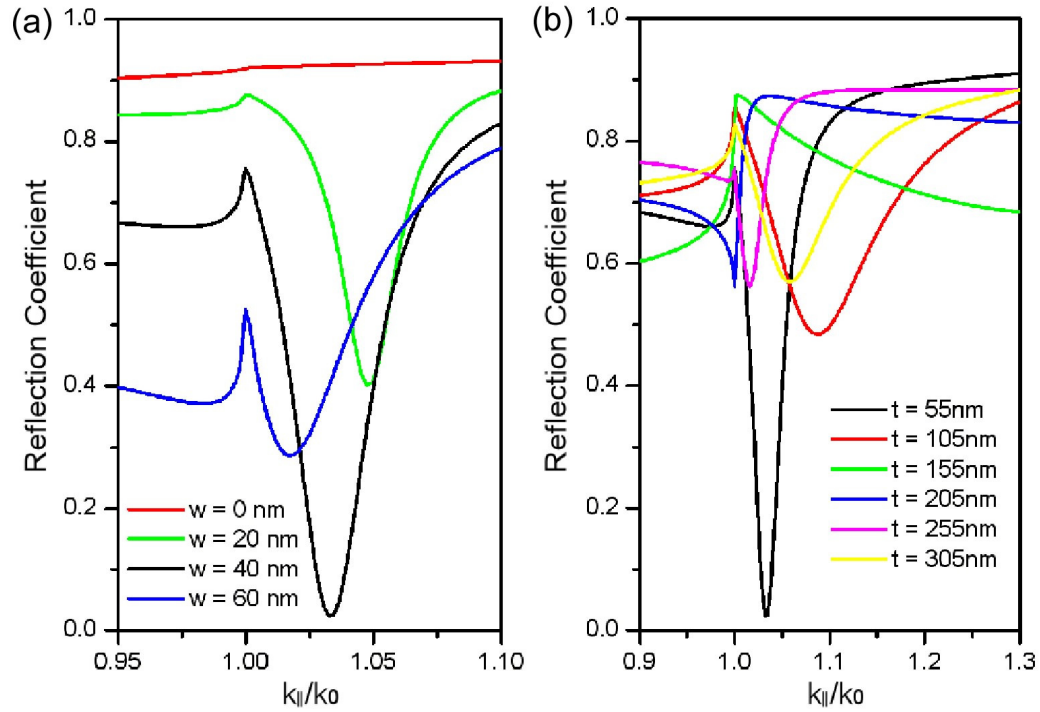
Fig. 4-2. Design of the plasmonic metamaterial: (a) Simulated reflection spectra at 640 nm with the fixed thickness d = 55 nm and period Λ = 140 nm, for different air slit widths w. (b), Simulated reflection spectra at 640 nm with the fixed period Λ = 140 nm and air slit width w = 40 nm, for different slab thicknesses d.

Computer simulations have been performed to validate the proposed TE to plasmon coupling and to optimize the geometry parameters of the designer plasmonic metamaterial. For simulations and experiments we choose to use visible wavelengths varying from 540 nm to 680 nm with a focus on a detailed study at the wavelength of 640 nm. Rigorous coupled wave analysis is employed to calculate reflection coefficients for a TE polarized plane wave incident from a high-index substrate (n = 1.5) side. The geometry is optimized to achieve minimum reflection coefficient which in turn corresponds to maximum excitation efficiency of SPPs. We consider the case where the incident wave vector (K_x, K_y, K_z), has an in-plane projection along the diagonal, such

that $K_x = K_y = k_{\parallel} / \sqrt{2}$, and $k_{\parallel}$ is the parallel wavenumber. Figs. 4-2(a) and 4-2(b) show

the reflection coefficient as a function of the parallel wavenumber of the incident wave

for different air slit widths and different slab thicknesses, respectively. We determine that

the optimal geometry has a period of Λ = 140 nm, slit width of w = 40 nm, and slab

thickness of d = 55 nm. The reflection coefficient is almost vanishing so that a nearly

perfect (100%) TE to plasmon coupling efficiency with polarization conversion was

achieved.

4.3 Analysis of Bloch modes in metamaterial

To gain deeper insight into the excitation mechanism of the TE-excited plasmon,

we investigate the electromagnetic Bloch eigen modes propagating in the positive and

negative z directions inside the metamaterial slab. As explained above, these modes are

hybrid, but since the slab is a periodic layered medium in the x direction, the modes are

either TM or TE with respect to x, denoted by TM_x and TE_x, respectively. The dispersion

relation for the Bloch modes that propagate inside the metamaterial slab are obtained by

imposing the boundary conditions at the interfaces, as well as the Floquet theorem with a

periodic phase corresponding to the incident wave vector. The dispersion relation is then

given by,

$$
\frac{(Z_a + Z_m)^2}{4 Z_a Z_m} \cos\left[k_{x,a} w + k_{x,m} (\Lambda - w) \right]
$$

$$
- \frac{(Z_a - Z_m)^2}{4 Z_a Z_m} \cos\left[k_{x,a} w - k_{x,m} (\Lambda - w) \right] = \cos\left(K_x \Lambda \right),
$$

(4.1)

where the wavenumbers in the x direction are $k_{x,i} = \sqrt{k_0^2 \varepsilon_i - K_y^2 - \beta_z^2}$, the impedances are

$Z_i = \eta_0 k_{x,i} / k_0 \varepsilon_i$ for TM$_x$ modes, and $Z_i = \eta_0 k_0 / k_{x,i}$ for TE$_x$ modes, ε_i are the

permittivities in each region, and $i = a, m$ for the air and metal, respectively; η_0 is the

vacuum impedance. The dispersion relation can then be solved to obtain the complex β_z

as shown in Fig. 4-3.
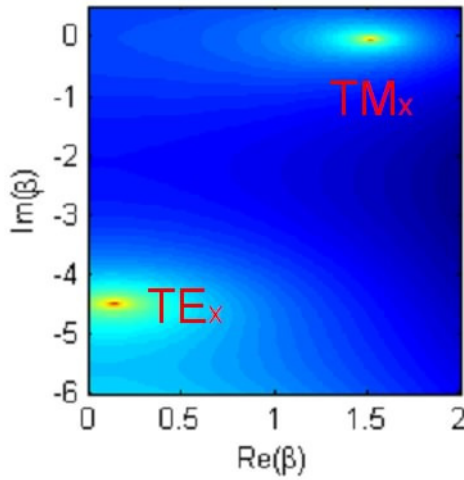
Fig. 4-3. Complex β_z plane shows the eigen values of Bloch modes inside slits of the metamaterial.

Table 4-1. Complex wavenumbers β_z normalized by k_0 in the z direction of the two lowest modes (TM$_x$ and TE$_x$) with different parallel wavenumbers k_{spp} for diagonal propagation of the designer SP, calculated at a wavelength of 640 nm.

Re(k_{sp}) mode	1.05 k_0	1.1 k_0	1.15 k_0	1.2 k_0	1.25 k_0
TM$_x$	1.512-0.046j	1.496-0.047j	1.479-0.048j	1.461-0.049j	1.442-0.051j
TE$_x$	0.120-2.616j	0.119-2.634j	0.118-2.654j	0.117-2.674j	0.115-2.695j

The lowest order mode is a TM$_x$ mode, which is a TEM-like mode in the slits.

The second mode is a TE$_x$ evanescent-like mode. Their complex wavenumbers β_z in the

z direction   vary   as   a   function   of   the   parallel   in-plane   wavenumber

$k_{\parallel} = k_{spp} = \sqrt{\left(K_x^2 + K_y^2\right)}$; values of β_z for $K_x = K_y$ are given in Table 1 for the two lowest

modes (TM$_x$ and TE$_x$) for different in-plane wavenumbers. The fundamental mode is

TM$_x$, and it has a dominant real part of its complex wavenumber β_z, such that it is

mainly propagating. The higher order TM$_x$ modes, however, as well as all TE$_x$ modes are

evanescent by nature, having a dominant imaginary part of β_z. Therefore, for large

thicknesses, the fundamental mode is almost solely responsible for the power transfer

above the slab, leading to the surface mode on the metamaterial surface.
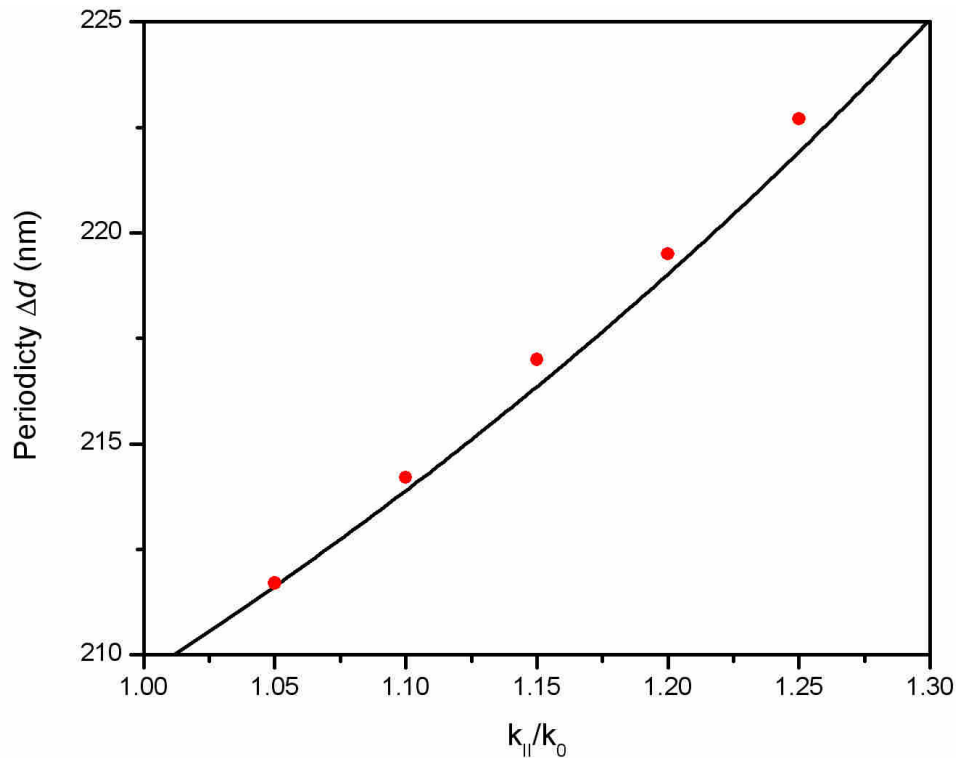
Fig. 4-4. The periodicity of the mode in thickness at different eigen vectors of SPPs retrieved from mode analysis (black) and simulations (red), exhibiting typical features of designer SPPs..

The angle of the dip viewed in reflection as a function of the slab thickness is thus

expected to be periodic with a period of half the effective wavelength

$\Delta d = \lambda k_0 / 2\,\mathrm{Re}\{\beta_z\}$. In other words, when increasing the thickness of the metamaterial

by Δd, the excited SP modes will have the same in-plane wavenumber. This is shown in Fig. 4-4, where this quantity is calculated according to values of β_z and compared with the exact period as a function of thickness variation. This periodic behavior is typical of designer SPPs [77].

4.4 Experimental fabrication and experimental setup

To fabricate the designed optimized subwavelength structure, we used focused-ion-beam milling of an Au film on a glass substrate. The SEM micrograph of the fabricated structure is shown in Fig. 4-5(b). The excited designer SPP modes in the fabricated metamaterial are characterized in reciprocal space by directly analyzing reflection images of SPPs' index ellipsoids in the k space as shown in Fig. 4-5(a) (see details in Chapter 3). These images are obtained from the glass substrate side of the sample inserted in an oil immersion microscope objective (MO) with a high numerical aperture (NA=1.4). A converging polarized spherical wave is used as an illumination function to code a wide-band angular spectrum of the illumination. The size of the obtained reflection image at the back focal plane is limited by the NA of our MO that corresponds to a free space wavenumber of $1.4\,k_0$. Note that the central dark ring in Figs. 4-6(a)-4-6(c) (i.e., image of the phase ring inside the phase contrast MO) obscures some information, but the information of interest in our study lies at larger wavenumbers. The dark tails (reflection dips) in the reflected images correspond to excitation of the designer SPPs, similarly to the Kretschmann-Raether configuration that uses prisms to excite SPPs, and represent information about their index ellipsoids.
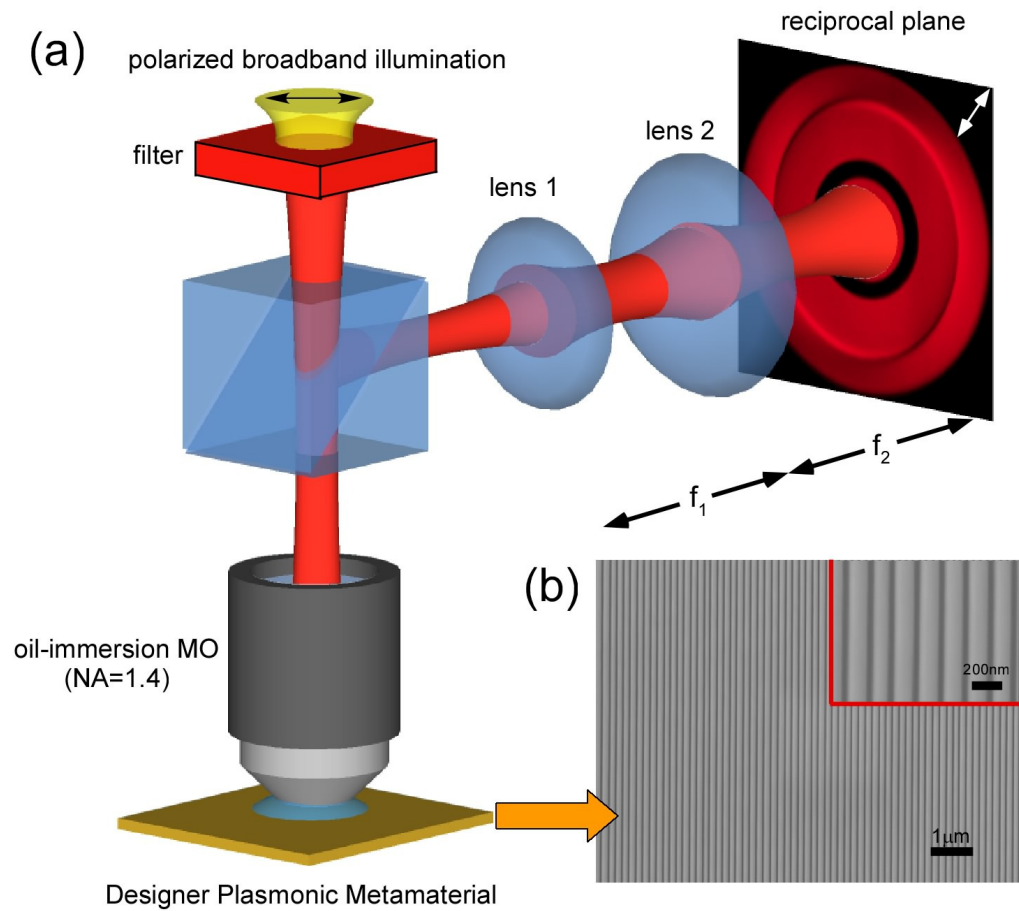
Fig. 4-5. Experimental configurations: (a), Measurement configuration that can directly capture the index ellipsoids by imaging the reflection in reciprocal space. (b), SEM micrographs of the fabricated metamaterial.
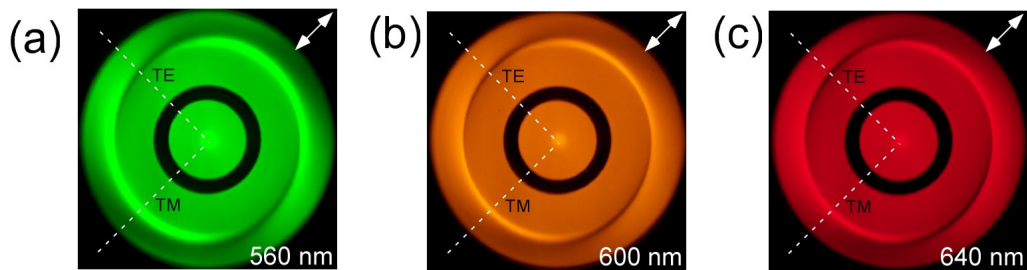
Fig. 4-6. Measured index ellipsoid of designer SPPs at (a) 560 nm, (b) 600 nm, (c) 640 nm.

These measurements are performed as a function of optical wavelength using a white light source in combination with a series of 10 nm bandpass interference filters in

the spectral range of interest, i.e., from 540 nm to 680 nm as shown in Figs. 4-6(a)-4-6(c) for wavelengths of 560 nm, 600 nm, and 640 nm, respectively. The polarizer is oriented at an angle of 45° with respects to the *x* direction. Therefore TM components are lying at the plane of 45°, while the incident plane of TE field is the plane of -45°. Thus the diagonals contain information about pure TE and TM components while the remainder of the space represents linear combinations of TE and TM incident waves. Since TE and TM are orthogonal, all the necessary information lies in the diagonals.

4.5 Extraordinary TE to plasmon coupling

The numerically simulated and experimentally measured index ellipsoids of the designer plasmon modes in reciprocal space are shown in Figs. 4-7(a) and 4-7(b), respectively, for a wavelength of about 640 nm. The detailed reflection spectra for TE and TM incidence have been extracted perpendicular (-45°) and parallel (45°) to the polarization, respectively, showing a good agreement between the experimental data and the simulation in Fig. 4-7(c). The extraordinary TE to plasmon coupling is observed as a sharp dip that occurs where its incident parallel wave vector satisfies the phase matching condition to excite the designer SPPs. However, in contrast to excitation of conventional SPPs, there is no pronounced dip in the reflectivity of TM polarization, indicating that surface waves are not generated. It is evident that a nearly perfect (100%) TE to plasmon coupling efficiency was achieved.
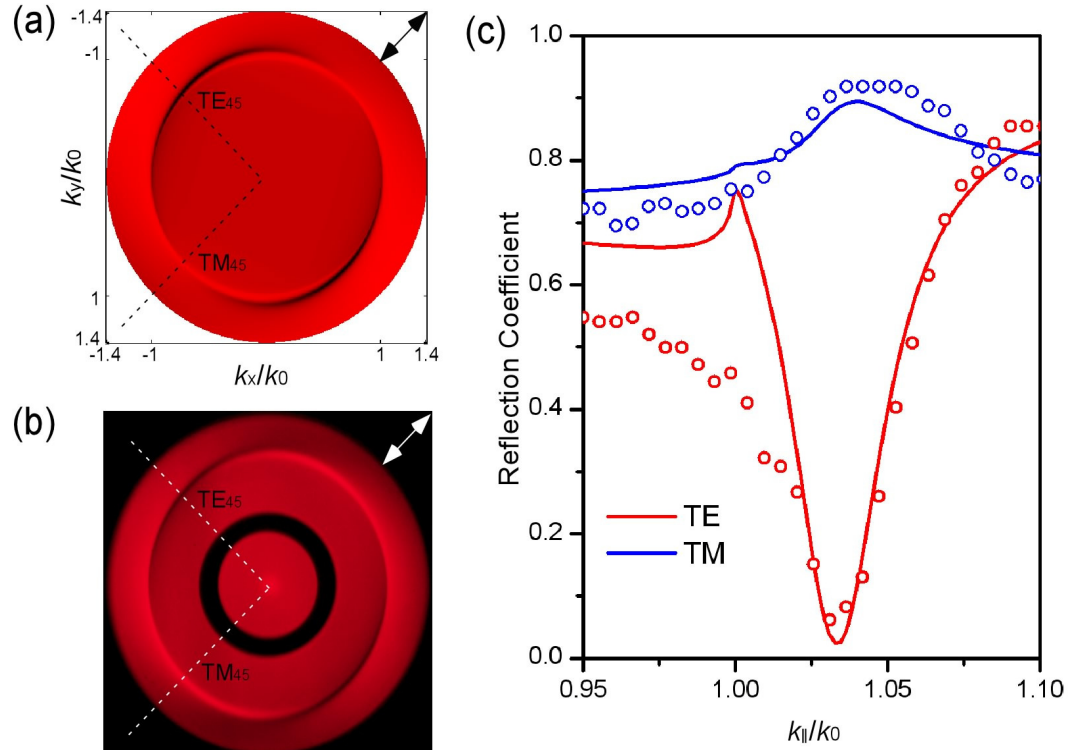
Fig. 4-7. Enhanced TE to plasmon coupling at 640 nm. (a), Simulated index ellipsoid of the excited surface mode in a representation of reflected power distribution in reciprocal space. (b), Experimental imaging of reflection from the metamaterial in reciprocal space. (c), Detailed reflection spectra retrieved from (a), (b) as TM (blue) is parallel and TE (red) is perpendicular to the incident polarization. Solid curves and hollow circles represent the results from simulation and experiment, respectively.

The inherent nature of the surface mode supported by this extraordinary TE-coupling has been further investigated using Finite Element Method (FEM) simulations, showing strong field confinement on the surface and exponentially decaying fields into the air, associated with this mode, as seen in Figs. 4-8(a)-4-8(c). Remarkably, although the polarization of the incident field is TE, the excited surface mode is almost entirely TM-polarized, as E_z and the magnetic field transverse to the direction of propagation $H_\perp$ are strongly dominant. The air slits act as a series of coupled transmission lines that efficiently transfer the power through the hybrid plasmonic modes (TM_x and TE_x) inside the metamaterial slab. TM-polarized components are generated due to the inherent hybrid

nature of these modes and provide highly efficient polarization conversion from the incident wave to the excited surface mode.
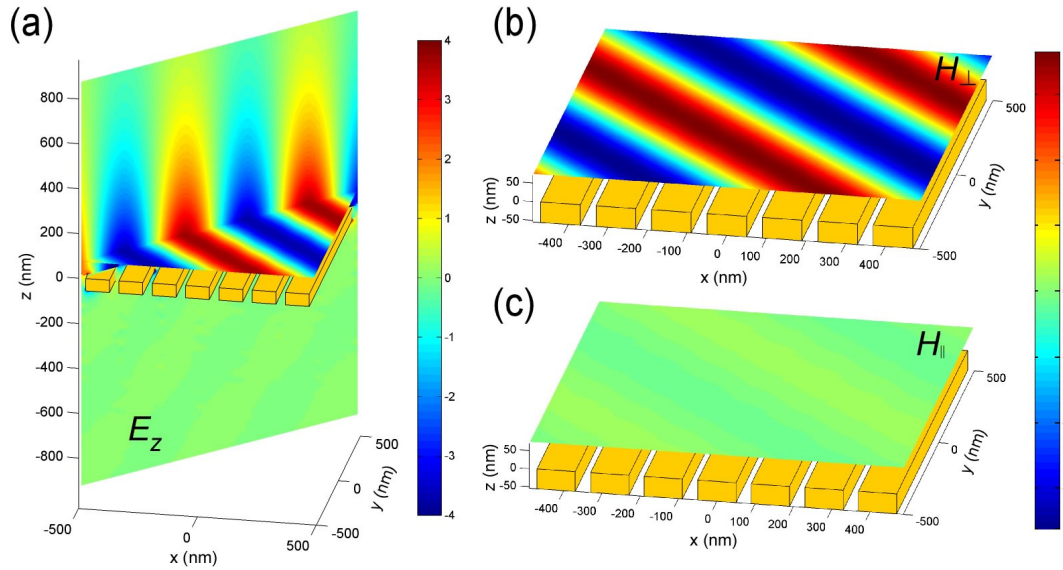
Fig. 4-8. FEM simulations of the excited surface mode by TE incidence. (a), Field distributions of E_z in the diagonal cross-section and x-y plane, respectively. (b), Field mapping of the in-plane magnetic field component transverse to k_{spp}, $H_\perp$ (TM component). (c), Field mapping of the in-plane magnetic field component parallel to k_{spp}, $H_\parallel$ (TE component), showing TM characteristics associated with designer SPPs.

Fig. 4-9 shows the dispersion relation of the designer SPPs. The experimentally measured wavevectors from Fig. 4-6 at different wavelengths are compared with the wavevectors obtained by numerical simulations, which are the locations of the dips in the simulated reflection spectra of TE incidence. Similarly to conventional SPPs, the designer SPPs are associated with larger wavevectors at shorter wavelengths, asymptotically approaching the effective surface plasma frequency [76-79]. In the range of interest, the experimental and theoretical results are found to be in very good agreement, manifesting a broadband extraordinary TE to plasmon coupling of our designer plasmonic metamaterial. Although the optimum design was performed for the

wavelength of 640 nm, high coupling efficiencies are obtained in a range of over 100 nm (i.e., 70% at 540 nm and 90% at 680 nm), showing broadband operation.
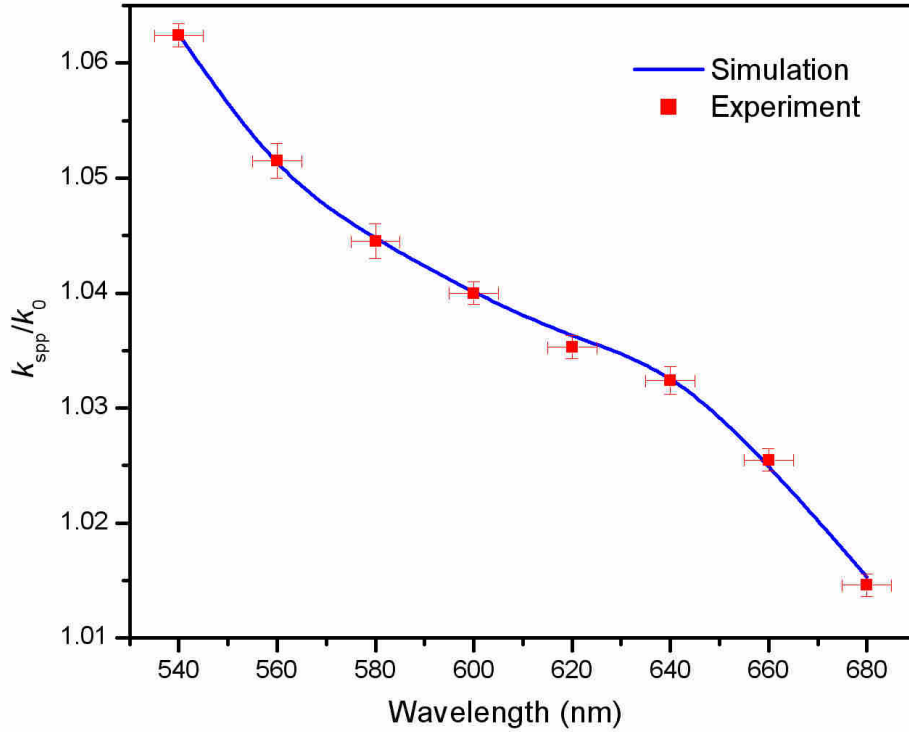
Fig. 4-9. Dispersion relation of excited designer SPP waves at the air/metamaterial interface. Solid curve and square markers correspond to data retrieved from numerical simulations and experimental measurements, respectively. For the experimental data, the error-bar in wavelengths indicates the bandwidth (10 nm) of the bandpass filters used in the experimental measurement.

4.6 Summary

The presented optical designer plasmonic metamaterial overcomes the inherent limitation of SPPs' TM-polarization nature and supports highly efficient broadband TE to plasmon coupling. Our results are promising for improving the overall plasmonic excitation efficiency in a wide range of applications, including plasmon-assisted photovoltaics and on-chip plasmonic circuits. While the investigated geometry in this

work varies only in two dimensions, the optical fields vary in all three dimensions. Thus the plasmonic hybrid modes that facilitate the demonstrated phenomena become hybrid, in contrast to previously investigated 2D problems. Further complication of the geometry of such optical metamaterials to variations in 3D offers significant possibilities for creating designer metamaterials with counterintuitive optical responses. Engineered in the 3D deep subwavelength "artificial molecules" of metamaterials, the plasmonic hybrid modes open a door to allow sophisticated nanometric linear and circular polarization mixing, as well as conversion and manipulation of optical guided and free space waves. This concept may be further extended to 3D layered structures [84, 85] by engineering the vertical connectivity between different layers, providing flexibilities in the design of novel nanophotonic structures.

4.7 Acknowledgements

Chapter 5 Plasmonic Photonic Crystal

5.1 Introduction

Photonic crystals are periodic optical nanostructures that are designed to affect the motion of photons in a similar way that periodicity of a semiconductor crystal affects the motion of electrons [86-88]. The strong photon scatterings can open a broad bandgap where the propagation of light is not allowed when the periodicity of photonic crystals is on the length scale of the wavelength. This property enables one to control light with amazing facility and produce effects that are impossible with conventional optics. The introduction of different defects can thus give rise to localized electromagnetic states: strong optical filed localization [89], linear subwavelength waveguiding [90], and other interesting applications.

Although unique SPP properties has led to myriad plasmonic applications, excitation and control of SPP fields has not yet been advanced in a systematic fashion as, for example, for optical fields in free space and dielectric waveguides. Recent work on Fourier plasmonics, starts exploiting both refractive [91, 92] and diffractive [93, 94] SPP devices. Moreover, SPP fields can be excited and manipulated by photonic crystal lattices (PCLs) similarly to that of light in photonic crystals made of dielectrics. For example, due to Bragg resonance at the boundaries of Brillouin zones, the SPP fields in a specified frequency range are forbidden to propagate through a periodic array of in-plane metallic bumps, which has been used to make waveguides with sub-wavelength confinement [95, 96], high-efficiency Bragg reflectors [97] and resonators [98] for SPP fields. However, it is difficult, if possible, to analytically calculate the band structure of these metallic

plasmonic photonic crystals (PPCs) using conventional methods like the plane wave expansion (PWE) method [99] and the multiple scattering theory [100].

In this chapter, we introduce a metallo-dielectric PPC, where the PCL is implemented in the dielectric material on the metal-dielectric interface. The band structure of the PPC has been theoretically calculated using the PWE method, exhibiting a complete wide two-dimensional (2D) bandgap for SPP fields. The experimental testing and numerical simulations of such a fabricated device confirm the band structure, validating our approach.

5.2 Design of plasmonic photonic crystal
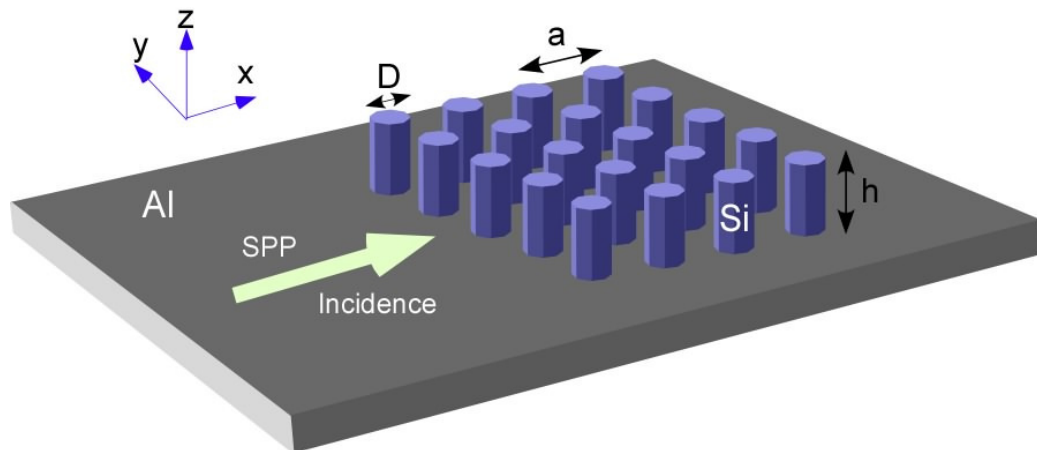
Fig. 5-1. Schematic diagram of PPC's geometry with design parameters a = 500 nm, D = 200 nm, and h = 400 nm.

Fig. 5-1 shows the structural geometry of our PPC design consisting of a 2D array of high dielectric constant Si cylinders surrounded by low dielectric constant air on the surface of Al. The Si cylinders are 200 nm in diameter and 400 nm in height, and they are arranged in a square mesh with a lattice constant $a = 500$ nm. Since Si-Al and air-Al interfaces have different effective indices for in-plane SPP waves, the equivalent

potential diagram in quantum mechanics would correspond to an electron propagating in a real crystal or light propagating in photonic crystals. This periodic potential contrast can cause strong scatterings near the boundaries of Brillouin zones, thus modifying SPP's dispersion and resulting in a complete bandgap caused by Bragg resonances.

For propagating SPP waves along the x direction (see Fig. 5-1), there are 3 field components: E_x, H_y and E_z, which can be expressed as,

$$E = E_0 \begin{pmatrix} jk_z/k_x \\ 0 \\ 1 \end{pmatrix} \exp(-jk_x x - k_z z), \tag{5.1}$$

$$H = -\frac{E_0 \omega \varepsilon(r) \mu_0}{k_x} \begin{pmatrix} 0 \\ 1 \\ 0 \end{pmatrix} \exp(-jk_x x - k_z z), \tag{5.2}$$

where $k_x = k_{spp} = k_0 \sqrt{\dfrac{\varepsilon_m \varepsilon(r)}{\varepsilon_m + \varepsilon(r)}}$, $k_z = \sqrt{k_x^2 - \varepsilon(r) k_0^2}$, and ε_m , $\varepsilon(r)$ are permittivities of Al

and air (or Si), respectively. These electric and magnetic field components are not independent as the eigenstate for one component is also the eigenstate for the other two components. Due to the boundary continuity, the E_z component has been chosen to form eigenfunctions and used to calculate the band structure of the PPC using the PWE method. Since most of SPP's energy is confined on the surface, it is therefore reasonable to simplify Eq. (5.1) to consider E_z at $z = 0$,

$$E_z(r) = E_0 \exp(-jk_{spp} \cdot r). \tag{5.3}$$

For in plane SPP propagation, as reported [93, 94], the effective wave vector can be expressed as k_{spp} with the still valid Helmholtz equation,

$$\frac{1}{\varepsilon_{spp}(r)}\left(\frac{\partial^2}{\partial x^2}+\frac{\partial^2}{\partial y^2}\right)E_z(r)=\frac{\omega^2}{c^2}E_z(r),\qquad(5.4)$$

where $\varepsilon_{spp}(r)=(\frac{k_{spp}}{k_0})^2=\frac{\varepsilon_m\varepsilon(r)}{\varepsilon_m+\varepsilon(r)}$. By expanding $E_z(r)$ and $\varepsilon_{spp}(r)$ in reciprocal space

using Bloch theory, the eigen function of our PPC can be derived as

$$\sum_{\vec{G}}\varepsilon_{spp}^r\left(\left|\vec{G}-\vec{G'}\right|\right)\left|\vec{k}+\vec{G}\right|\left|\vec{k}+\vec{G'}\right|E_z(\vec{G})=\frac{\omega^2}{c^2}E_z(\vec{G}).\qquad(5.5)$$
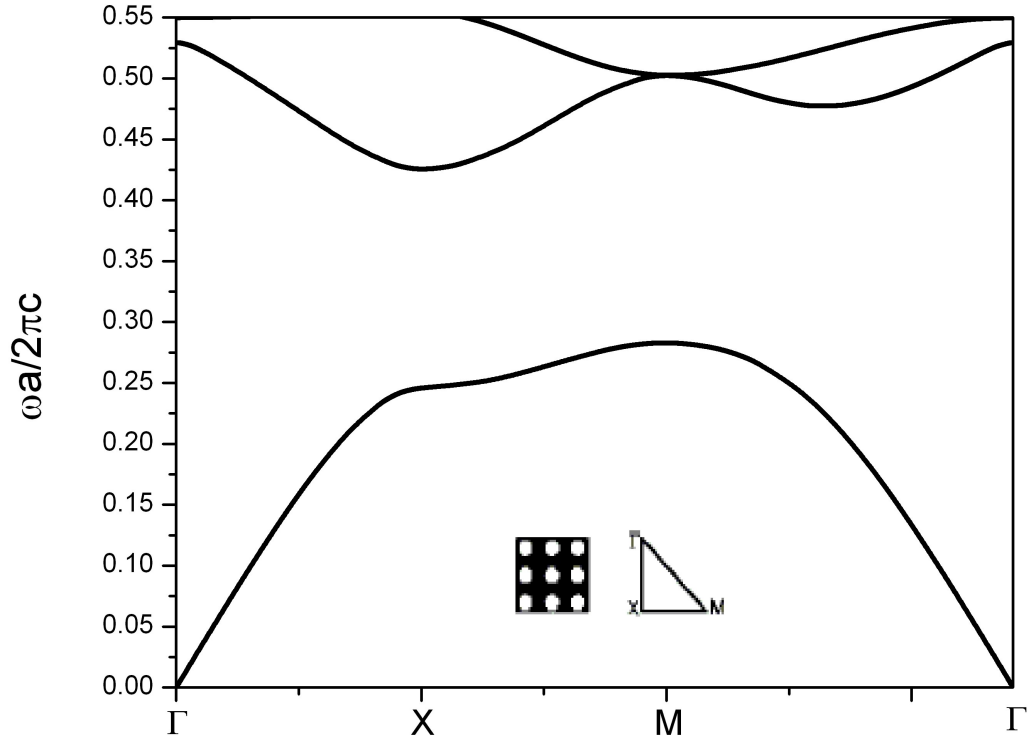
Fig. 5-2. Calculated band structure of the proposed PPC using the PWE method with 289 plane waves. A $0.14\,\omega a/2\pi c$ -wide 2D complete bandgap can be observed from $0.28\,\omega a/2\pi c$ to $0.42\,\omega a/2\pi c$.

For simplicity, we use Drude model for the permittivity of Al and since the band structure is only determined by the real part of the permittivities [101], we do not

consider the imaginary part of the permittivity ($\varepsilon_m = 1 - \dfrac{\omega_p^2}{\omega^2}$, where the plasma frequency

ω_p is 2.24×10^{16} rad/s) [102]. The permittivities of air and Si are set 1 and 12.4,

respectively. The calculated band diagram (see Fig.5-2) shows a complete $0.14\,\omega a / 2\pi c$-

wide 2D bandgap from $0.28\,\omega a / 2\pi c$ to $0.42\,\omega a / 2\pi c$. The complete 2D bandgap results

from high contrast between air and Si cylinders in $\varepsilon_{spp}(r)$.

This band structure is next validated by full wave 3-dimensional (3D) finite

element simulations (with 400 nm-high Si cylinders on the Al surface) using Comsol

Multiphysics 3.4 as shown in Figs. 5-3(a)-5-3(c). An SPP wave, propagating from left to

right, is launched at the left side of the simulation region. The periodic boundary

condition is implemented in the vertical direction and the perfect matched layer boundary

condition is applied on all other boundaries to eliminate the reflection. The permitivitty of

Al is still described by the Drude model ($\varepsilon_m = 1 - \dfrac{\omega_p^2}{\omega(\omega - j\gamma)}$) but with a damping

coefficient $\gamma = 1.22 \times 10^{14}$ rad/s [101]. We observe (see Figs. 5-3(a) and 5-3(c)) that the

SPP wave can propagate inside the PPC in the second and the first bands at the

frequencies of $0.48\,\omega a / 2\pi c$ and $0.22\,\omega a / 2\pi c$. But in the bandgap occurring at the

frequency of $0.39\,\omega a / 2\pi c$ (see Fig. 5-3(b)), strong attenuation can be observed and the

SPP field propagation is forbidden.
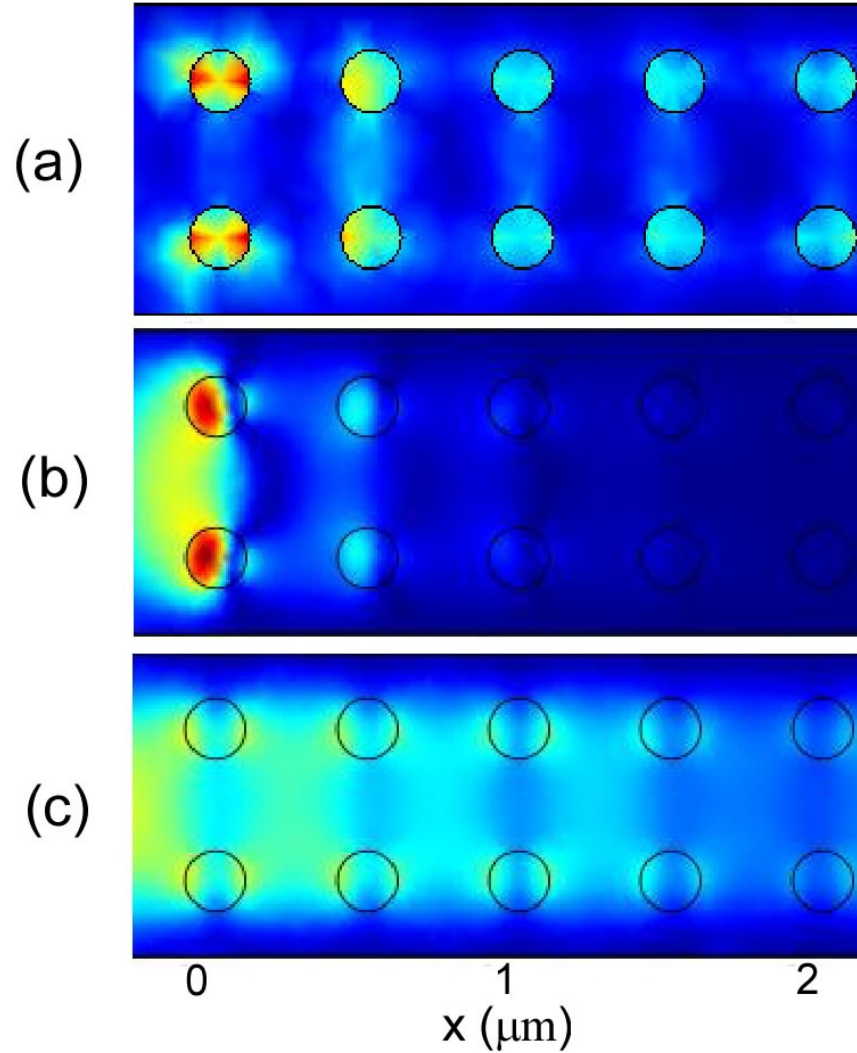
Fig. 5-3. Full wave 3D finite element simulations show $|H_y|$ of SPP waves propagating inside the proposed PPC at different frequencies: (b) $0.48\,\omega a/2\pi c$ (corresponding to the 2nd band); (c) $0.39\,\omega a/2\pi c$ (corresponding to the bandgap); (d) $0.22\,\omega a/2\pi c$ (corresponding to the 1st band).

5.3 Experimental fabrication

For experimental validations we fabricated the sample using standard overlay E-beam lithography method with the following steps as shown in Fig. 5-4: (1) A glass substrate was first cleaned and then coated with 5 nm thick Ti and 100 nm thick Al films; (2) a 1.5 μm thick polymethyl methacrylate (PMMA) layer was spun onto the metal plate and the designed PPC features were defined in PMMA by E-beam writing; (3) a 400 nm

thick film of amorphous Si was deposited over the PMMA mask; (4) using acetone lift-off procedure, the Si-based PPC was formed on the Al film surface; (5) the entire sample was covered again with a 200 nm thick PMMA layer for the fabrication of two nanohole arrays, one to the left and the other to the right of the SPP PPC; (6) the PMMA was E-beam patterned to create 200 μm × 200 μm nanohole arrays on a 1.6 μm square grid and with average nanohole diameter of 300 nm ; (7) the nanohole arrays were transferred to the Al film by wet chemical etching (E6 Metal Etchant), and PMMA was then removed using acetone.
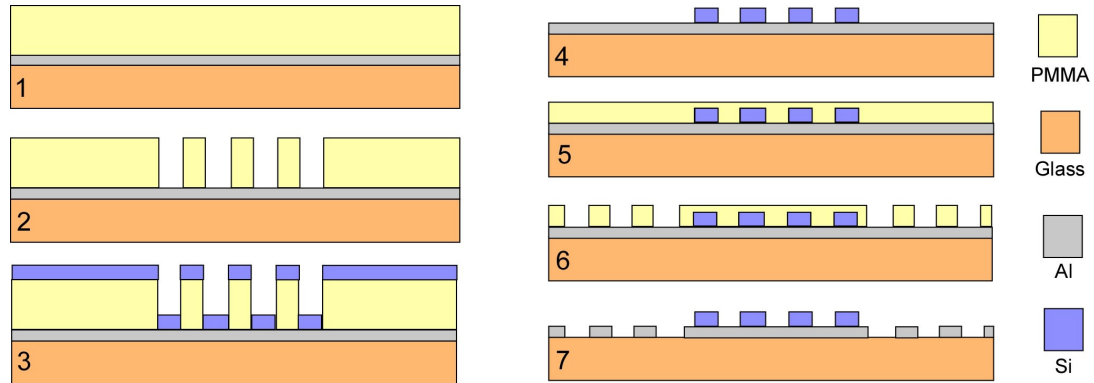
Fig. 5-4. Overlay E-beam lithography process to fabricate the designed PPC integrated with two nanohole arrays.

The fabricated PPC consists of 20 and 80 lattice elements in the longitudinal and the transverse directions of the propagating SPP field, respectively. The SEM micrograph of the Si-based PPC on the Al film is reproduced in the inset of Fig. 5-5. As shown in Fig. 5-5, there are two identical nanohole arrays integrated at different sides of the PPC for excitation and detection of SPPs: array #1 is used to couple light into SPPs and the excited SPP wave is normal incident to the PPC, and array #2 is used to couple SPPs back to the free space for the detection of the transmitted SPP wave through the PPC lattice.
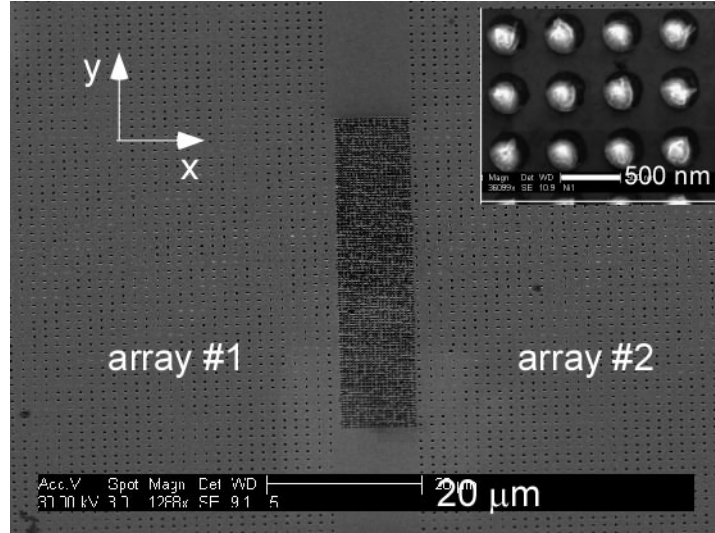
Fig. 5-5. SEM micrographs of the integrated structure consisting of nanohole array #1, a PPC, and nanohole array #2: the PPC is fabricated by deposition of amorphous Si on Al/air interface; nanohole arrays #1 and #2 are fabricated in Al film and used for excitation (left) and detection (right) of the corresponding incident and transmitted through the PPC lattice SPP fields.

5.4 Characterization results

The integrated device was characterized using our far-field SPP detection system at the wavelength of 1520 nm ($0.33\,\omega a/2\pi c$) [31, 32], as shown in Fig. 5-6. Incident light used for excitation of SPP waves in nanohole array #1 was polarized at 45° in the Cartesian coordinate system of the nanohole array grid. A 20X microscope objective (MO) is used to generate a narrow incident SPP beam on array #1. The SPP field transmitted through the PPC was radiated on nanohole array #2 and the scattered free space modes were collected by a 10X MO, transmitted through an orthogonally oriented polarization analyzer and imaged by a lens onto a charge-coupled detector (CCD) camera for detection and analysis. The pair of the crossed polarizer and analyzer is to increase the signal to noise ratio by removing the directly transmitted light.
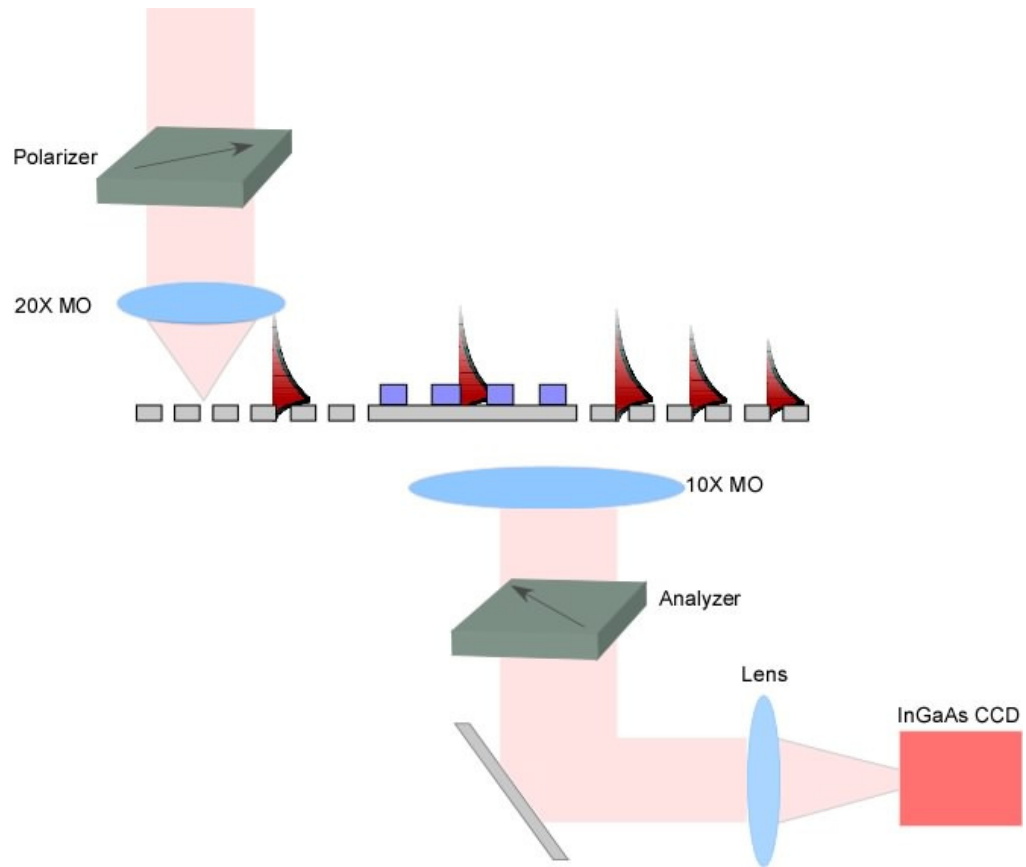
Fig. 5-6. Experimental setup that measures the transmission characteristics of PPC for SPP waves .
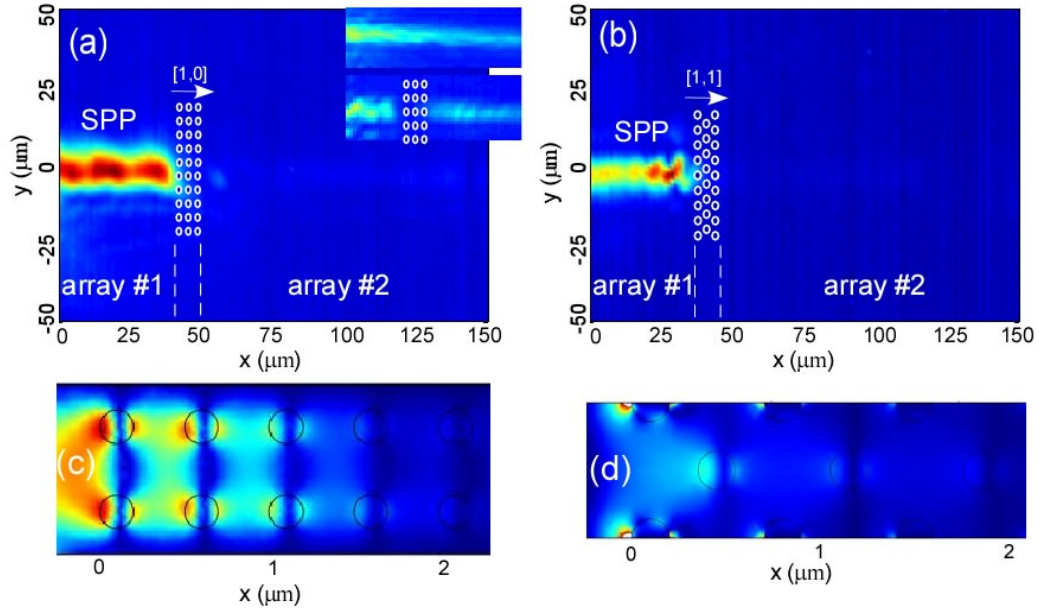
Fig. 5-7. (a), (b) Measured SPP time-averaged intensity maps as the SPP field is excited in nanohole array #1, propagates through the PPC and the transmitted SPP scatters from nanohole array #2 at 1520 nm ($0.33\,\omega a/2\pi c$). (c), (d) Numerical mappings of |H_y| of SPP waves propagating inside the proposed PPC at $0.33\,\omega a/2\pi c$. The SPP waves are incident along the PPC's lattice orientations: (a), (c) [1, 0] and (b), (d) [1, 1]. The insets in (a) represent the unperturbed SPP propagation on a continuous nanohole array (top) and SPP's propagation through a PPC with $a = 1000$ nm (thus the working wavelength is located in the first band) (bottom). Note that the simulations in (c) and (d) use periodic boundary conditions and provide insight to the field penetration into the PPC lattice, showing performance consistent with experimental results.

The experimental validations for both [1, 0] (Γ-X) and [1, 1] (Γ-M) PPC lattice orientations and their comparisons with computer simulations are summarized in Fig. 5-7. Figs. 5-7(a) and 5-7(b) show the measured SPP time-averaged intensity maps as the SPP field is excited in nanohole array #1, propagates through the PPC and the transmitted SPP scatters from nanohole array #2 (see the labeled regions). The width of the excited SPP beam is about 10 µm-wide and its convergence is well controlled within a half-angle of 2°. Note that the SPP excitation spot in nanohole array #1 is not in the field of view of the images shown in Figs. 5-7(a) and 5-7(b), (i. e., the excited SPP waves enter the left boundaries on the images). The PPCs in Figs. 5-7(a) and 5-7(b) are fabricated for

operation with normally incident SPP fields to propagate along [1, 0] (Γ-X) and [1, 1] (Γ-M) orientations of the PPC lattices, respectively. Since the ratio between the measured out-coupled intensities can represent the ratio between SPP energies at different spots, we calculated, from the experimental data, the ratio between out-coupled SPP intensities at two spots, right before and after the PPC, to evaluate the transmission coefficients. The measured transmittances are about 5.4% and 5.8%, respectively, that are about 6 times less than the transmittance observed with a 400 nm high Si slab on an Al surface. To have visual comparisons, the insets in Fig. 5-7(a) show the image of unperturbed SPP propagation on a continuous nanohole array (top) and SPP's transmission through the first passing band of another PPC with $a = 1000$ nm. For both PPC orientations shown in Figs. 5-7(a) and 5-7(b), the incident SPP waves can not propagate through the PPC, since the wavelength of 1520 nm ($0.33 \omega a / 2\pi c$) lies within the complete band gap of the PPC as expected from Fig. 5-2. Numerical simulations in Figs. 5-7(c) and 5-7(d) also confirm our measured results, showing strong attenuation inside the PPC for both lattice orientations. However, it should be noted that compared to numerical simulation at $0.33 \omega a / 2\pi c$ (see Fig. 5-3(b)), the SPP fields at $0.33 \omega a / 2\pi c$ decay slower (see Fig. 5-7(c)) although the value $0.33 \omega a / 2\pi c$ lies closer to PPC's midgap frequency. This might be due to lower effective index caused by finite height of Si cylinders that is about 4 times shorter than the SPP's evanescent tail extending into the dielectric medium. Lower effective index can cause blue shift of PPC's band structure. Since the propagation of the SPP waves is inhibited in both [1, 0] (Γ-X) and [1, 1] (Γ-M) orientations of the PPC

lattices, it is evident, both theoretically and experimentally, that our PPC contains a complete 2D bandgap for in-plane SPP fields.

5.5 Conclusion

In summary, a PPC, that can modulate the propagation of in-plane SPP waves, has been designed, fabricated, and validated experimentally. The band structure has been calculated using the PWE method with proper approximations. It shows a complete $0.14\,\omega a/2\pi c$-wide 2D band gap. This complete band gap is verified by full wave 3D numerical simulations using the actual geometry of the fabricated device, and confirmed by experimental characterizations. For the future, our metallo-dielectric approach to PPC with an appropriate design of the desired band structure will allow more accurate design and realization of PPC-based on-chip waveguides, reflectors and resonators. In addition, numerous phenomena that have been observed in conventional dielectric photonic crystals, including super-prism [103], self-collimation [104], and negative refraction [105] can be also demonstrated for SPP waves.

5.6 Acknowledgements

The text of Chapter 5, in part or in full, is a reprint of the material as it appears in the following publication:

Liang Feng, Ming-Hui Lu, Vitaliy Lomakin, and Yeshaiahu Fainman, "Plasmonic Photonic Crystal with a Complete Bandgap for Surface Plasmon Polariton Waves," Applied Physics Letters **93**(23)**,** 231105 (2008).

The dissertation author was the primary researcher and the co-authors listed in this publication directed and supervised the research which forms the basis for this chapter.

Chapter 6   Fourier Plasmonics

6.1 Introduction

One unique property of the SPPs is their high confinement near the interface and intrinsically localized in a small volume, recently widely utilized in optical devices for subwavelength electromagnetic wave-guiding, label-free biochemical sensing, nano-photolithography and data storage. SPP-based S-bends, Y-splitters, Mach-Zehnder interferometers and waveguide-ring resonators have also been demonstrated [106, 107]. Additionally, SPP wavelength can be shorter than the wavelength of light in surrounding media, leading to applications in sub-diffraction-limited in-plane microscopy. Sub-diffraction-limited imaging can in principle be realized by negative refractions to recover the high spatial frequency information carried by the evanescent wave. However, in-plane SPP microscopy offers, arguably, a more promising alternative to accomplish this goal due to the challenge in fabricating negative refraction materials in the visible spectrum. In the past, far-field microscopy combined with the in-plane image magnification by SPP, was suggested [108]. More recently, an negative refraction SPP hyperlens was implemented with resolution on the order of $\lambda_0/7$, far beyond the diffraction limit [109]. However, the challenge remains to excite and control propagating SPP fields in a systematic fashion as is possible with optical fields both in free space and dielectric waveguides. For example, it would be of great interest in biomedical research to create a confocal microscope with sub-diffraction limited resolution exploiting focused SPP fields.

To date, several groups have demonstrated for SPP focusing. A converging SPP wave has been obtained by coupling a laser beam to SPP via an array of concentrically arranged circular metallic slits [110, 111], other in-plane structures [112, 113], or by coupling a converging beam via a 2-dimensional rectangular nanohole array [32]. SPPs have also been localized at the sharp end of a tapered plasmonic waveguide [114-116]. Other authors have used refractive elements (e.g. a traditional lens [91] or a negative refraction superlens [117]) placed directly on top of the metallic film to focus SPP waves by introducing quadratic phase. In this Letter, we report another focusing approach using an in-plane SPP Fresnel zone plate (FZP) [118]. We provide design rules for the construction of such an FZP, and demonstrate experimentally the diffractive focusing of SPP fields in the plasmonic structures fabricated according to these design rules.

6.2 Design and fabrication of in-plane SPP FZP

A conventional optical binary amplitude FZP consists of a series of concentric rings, known as Fresnel zones that alternate in transmittance between transparent (i.e., 1) and opaque (i.e., 0). An adaptation of FZP for in-plane SPP focusing is illustrated schematically in Fig. 6-1. Consider the diffraction of an SPP plane wave impinging on this structure from the left. Constructive interference of SPP fields is obtained at a focal distance f from the FZP when Fresnel zone radii r_m satisfy

$$ r_m = \sqrt{m\lambda_{spp}f + \frac{m^2\lambda_{spp}^2}{4}} \, , \tag{6.1} $$

where m is an integer, and λ_{spp} is the SPP wavelength. For a planar FZP, r_m are boundary positions where transmittance changes between transparent and opaque.
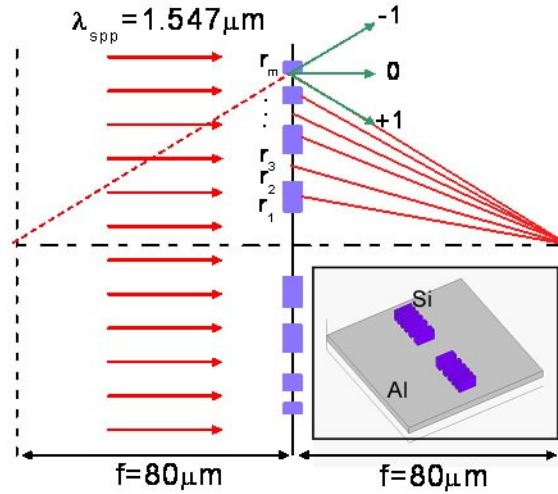
Fig. 6-1. Schematic diagram of SPP FZP geometry and design parameters.

In our experiments, a 12-zone SPP FZP with zone radii given by Eq. (1) was constructed at an Al/air interface for operation at a free space wavelength of 1.55 μm (corresponding to λ_{spp} = 1.547 μm) and a focal length f =80 μm. As in previous work [31, 32], nanohole arrays were integrated on both sides of the device for launching SPP waves and visualizing their propagation.

The sample was fabricated by standard overlay E-beam lithography as that in Chapter 5: (1) A glass substrate was first cleaned and then coated with 5 nm thick Ti and 100 nm thick Al films; (2) a 1.5 μm thick polymethyl methacrylate (PMMA) layer was spun onto the metal plate and 5 μm wide FZP features were defined in PMMA by E-beam writing; (3) a 400 nm thick film of amorphous Si was deposited over the PMMA mask; (4) using acetone lift-off procedure, the Si-based FZP was formed on the Al film surface; (5) the entire sample was covered again with a 200 nm thick PMMA layer for the fabrication of two nanohole arrays, one to the left and the other to the right of the SPP FZP; (6) the PMMA was E-beam patterned to create 200 μm × 200 μm nanohole arrays on a 1.6 μm square grid and with average nanohole diameter of 300 nm; (7) the nanohole

arrays were transferred to the Al film by wet chemical etching (E6 Metal Etchant), and PMMA was then removed using acetone. SEM micrographs of the final product, showing the FZP and both nanohole arrays on the Al film, are reproduced in Fig. 6-2.
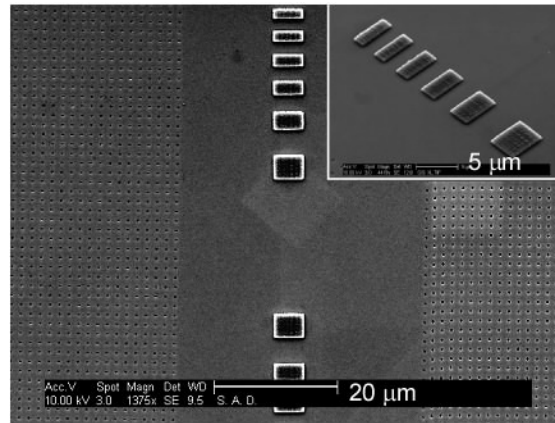
Fig. 6-2. SEM micrographs of SPP FZP fabricated by deposition of amorphous Si on Al/air interface; also seen are the integrated arrays of nanoholes in the Al film for SPP field excitation (left) and detection (right).

6.3 Characterization of diffractive focusing of in-plane SPPs

The fabricated in-plane SPP FZP was tested with our far-filed spatial imaging technique operating with mode-locked 200 fs ultrashort laser pulses at a center wavelength of 1.55 μm, as shown in Fig. 6-3. The average field intensity map of SPPs was first taken to characterize SPPs diffractive focusing due to the FZP.
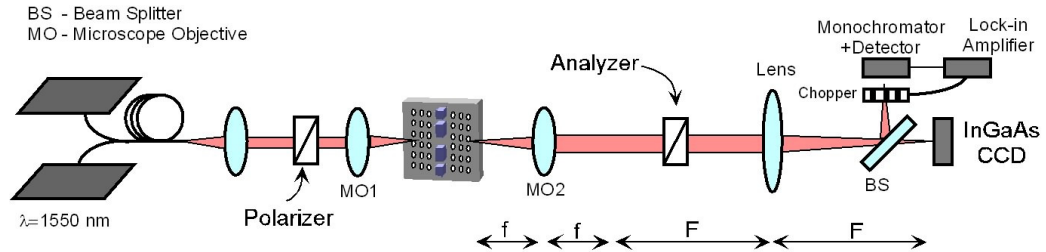
Fig. 6-3. Experimental setup for far-field imaging of in-plane SPP propagation via the grating coupling method.

Incident light was polarized at 45° to the nanohole arrays, and re-radiated field was detected with an orthogonally oriented polarization analyzer. Laser light was focused through a 5X microscope objective onto the input nanohole array to the left of the FZP at normal incidence. The lattice constant of hole arrays was chosen close to the SPP wavelength so that [±1, 0], [0, ±1] SPP modes were excited, with [1,0] mode directed toward the FZP. The incident SPP was converging at a half-angle of 2°, negligible compared to the 27° convergence half-angle introduced by the FZP. (The alignment of the objective was verified using a different area of the same sample). The excited SPP wave had a transverse width of about 80μm. Diffraction at the SPP FZP and subsequent interference resulted in focusing of the transmitted SPP at a particular location in the area of the output nanohole array to the right of the FZP. This detection nanohole array caused SPP to radiate into far field, where an image was finally captured with a 10X microscope objective coupled to a CCD camera.
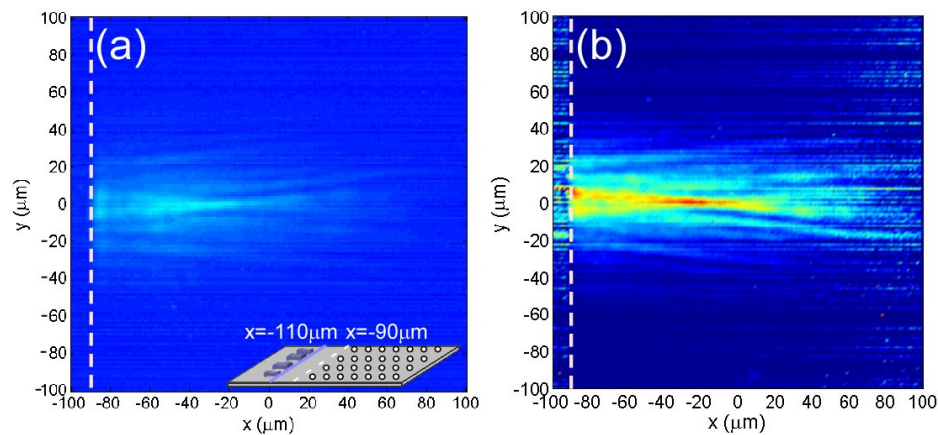
Fig. 6-4. (a) Measured SPP time-averaged intensity map over the nanohole array to the right of the FZP, showing +1-st order diffractive focusing and -1-st order diffractive fringes. Dashed white line indicates the left edge of the nanohole array. The FZP is located at x=-110 μm. Inset: Schematic diagram of the FZP and the nanohole array. (b) Post-processed image obtained from (a) by compensating for radiative loss.

The result of this measurement, shown in Fig. 6-4(a), represents the intensity map of SPP over the output nanohole array. The +1st-order FZP focal point is clearly seen at $x = -27$ μm, 83 μm away from the FZP (located outside the image at x=-110 μm, 20 μm to the left of the white dashed line indicating the edge of the nanohole array). The 83 μm measured focal length is in good agreement with the 80 μm expected from Eq. (6.1). Fringes due to the diverging -1st-order of the FZP are also visible.

The intensity map in Fig. 6-4(a) also reveals the rapid attenuation of SPP waves as they propagate from left to right across the nanohole array. The second nanohole array is introduced only for visualization purposes, and, in principle, would not be necessary in in-plane imaging applications. It is therefore informative to compensate for the radiation losses caused by this array in post processing. To this end, we assumed that, absent radiation and material loss, the SPP's energy flow would be conserved, i.e., the integration of the measured intensity of the scattered SPP waves along the y direction would be the same at different x locations. Then the calculated material loss of Al (SPP propagation length ~322.5 μm at 1.55 μm wavelength) was added back to show the SPP intensity map predicted without the radiation loss in the area of the detection nanohole array. It is seen in Fig. 6-4(b) that, if the detection nanohole array is not present, SPP intensity at the focal point may be expected to be about 3 times that of the input SPP wave.

6.4 Analysis using conventional Fourier optics

The effectiveness of the in-plane SPP FZP described in this Chapter is limited somewhat by the fact that even its opaque zones are partially transparent. This is due to

the technical difficulty of fabricating Si-based FZP higher than several microns using the lift-off method in our fabrication technique. The evanescent tail of SPP fields in air extends further than the height of the FZP, and therefore a fraction of the incident SPP fields is able to transmit through the FZP opaque zones. Consequently, part of the SPPs "sails over" the Si barrier, the designed opaque zones of the in-plane SPP FZP. Experimentally, about 30% transmission was observed through those 'opaque' zones of FZP, a figure consistent with our finite-element numerical simulations. This defect can be taken into account by generalizing the standard Fourier optics expression for the FZP diffracted fields [108] to include contributions from both the transparent and the opaque zones of the FZP,

$$u(x, y) = \frac{\exp(ik_{spp}x)}{i\lambda_{spp}x} \iint_T u_0(y_0) \exp(\frac{ik_{spp}}{2x}(y - y_0)^2) dy_0$$

$$+ \frac{\exp(ik_{spp}x)}{i\lambda_{spp}x} \iint_O \sqrt{0.3} u_0(y_0) \exp(\frac{ik_{spp}}{2x}(y - y_0)^2) dy_0. \qquad (6.2)$$

SPP intensity $|u(x, y)|^2$ at the focal plane ($f = 80 \, \mu$m) calculated from Eq. (6.2) is plotted in Fig. 6-5(a), and agrees well with the measured result in Fig. 6-5(b) that was taken from the transverse direction at the focusing spot in Fig. 6-4(a). The data shown in Fig. 6-5 are normalized by the maximum values in the figure, i.e., the intensity of the focusing spot. The reasons for the small discrepancy probably include the error of Fresnel approximation due to steep focusing geometry, and the rough estimate of the transparency of the opaque FZP zones. Therefore, methods of conventional Fourier optics can be applied to describe in-plane diffraction of SPP waves, providing possibilities of miniaturizing bulky optical devices on plasmonic chips.
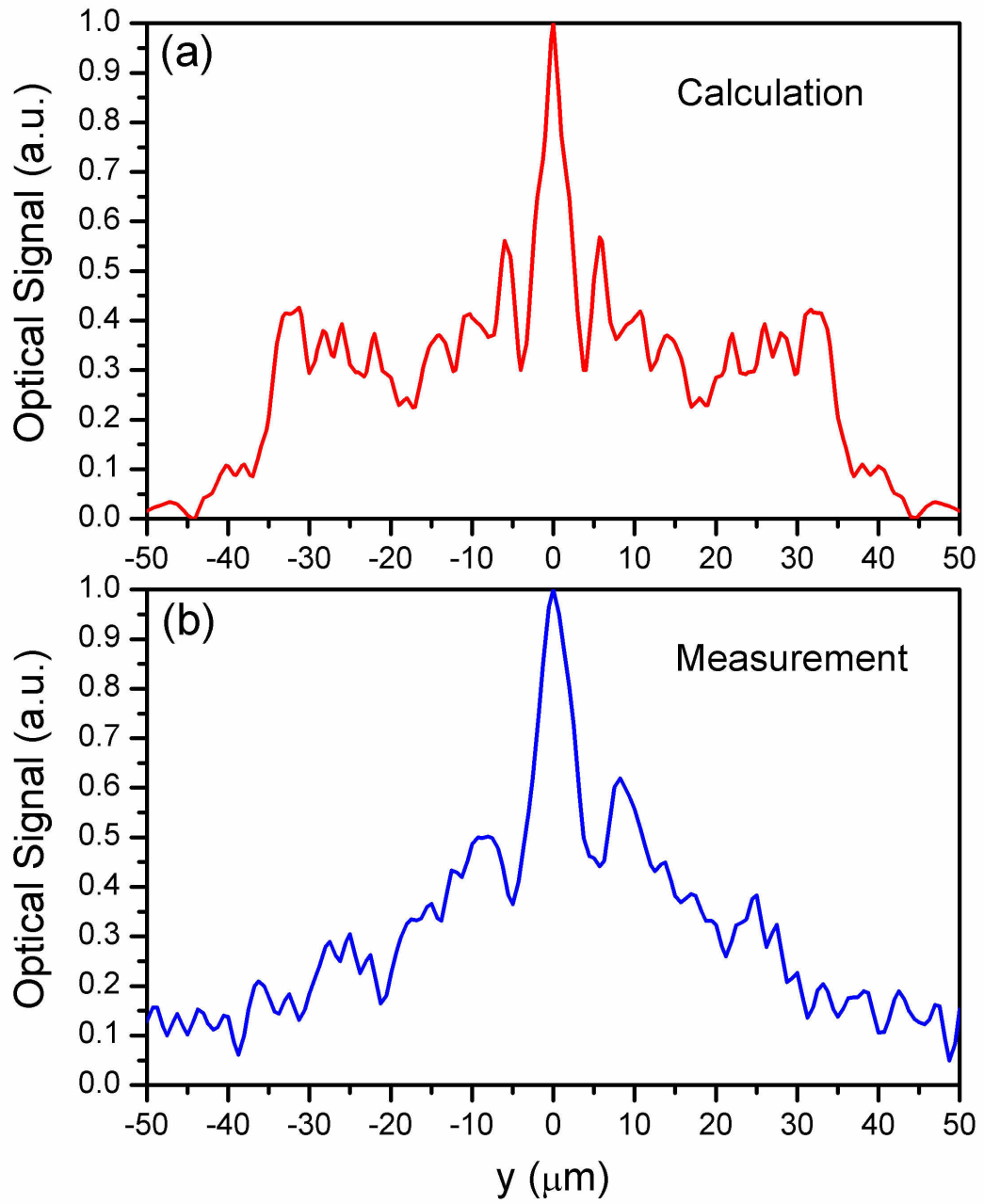
Fig. 6-5. SPP intensity profile in the focal plane computed by the Fresnel diffraction method (a) and found experimentally (b).

6.5 Temporal-spatial measurement of in-plane SPP focusing
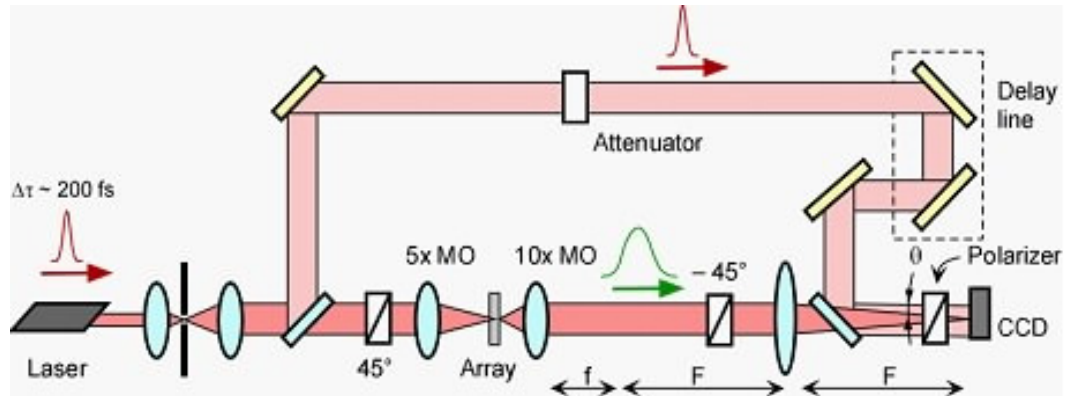
Fig. 6-6. Experimental setup incorporating a ultrashort pulse laser for temporal-spatial amplitude measurement of SPP waves.

In addition to average power measurement (Figs. 6-4 and 6-5), temporal-spatial amplitude distributions of the SPP waves were further investigated with our time-resolved spatial heterodyne imaging technique as shown Fig. 6-6 [32]. Interference patterns between a reference beam and far-field radiation of SPP passing over the nanohole array were captured at 150 different time delays, with about 6 fs separation between adjacent frames.
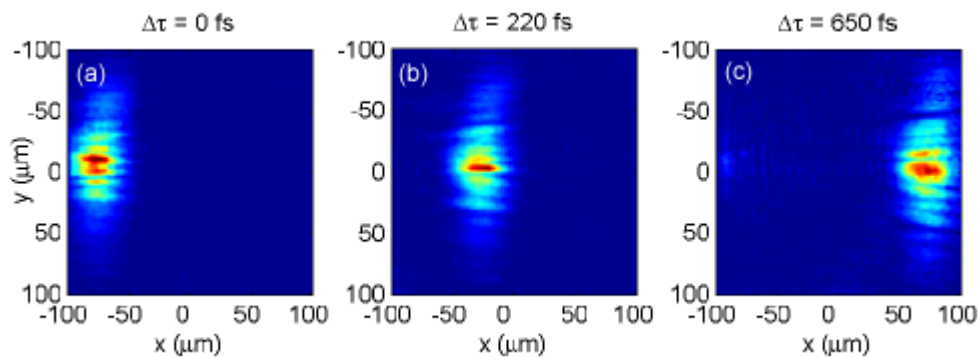
Fig. 6-7. Temporal evolution of spatial amplitude of the scattered SPP fields from the detection nanohole array (ranging from x=-100 μm to x=100 μm). (a) The converging SPP wave observed when the SPP pulse just enters the hole array. (b) The SPP pulse reaching its focal point after about 220 fs. (c) The SPP pulse diverging past the focal point.

Figs. 6-7(a)-6-7(c) show field magnitude spatial maps at times τ =0 fs, 220 fs, and 650 fs. Propagation of the SPP wavepacket from left to right over time is clearly visualized. The packet is also seen to converge to the optical axis at the focal point and diverge again thereafter. We also observed that the SPP focal spot can be moved by slight adjustment of the angle of incidence and the quadratic phase of the incident laser beam. This phase-controlled strategy can be helpful for in-plane microscopy applications.

6.6 Conclusion

In summary, an in-plane FZP for diffractive focusing of SPP fields on an Al/air interface was designed and fabricated. In-plane diffractive focusing of SPP was demonstrated and quantitatively characterized. The temporal and spatial characteristics of the focused SPP fields were experimentally analyzed using time-resolved spatial-heterodyne imaging technique. The measured time-resolved spatial amplitude images provide additional insight and confirm both the analysis and the measured average power results. The FZP focused SPP fields down to a focal point on a flat metallic film surface and concentrated the incident power of the SPP. This power concentration may help improve the contrast and longitudinal resolution of SPP in-plane microscopy, as well as facilitate interesting SPP-based nonlinear effects such as surface enhanced Raman scattering (SERS) [115]. In addition to the refractive plasmonics, our work on SPP diffraction, leads to a direction of research on Fourier plasmonics, exhibiting great opportunities and capabilities of miniaturizing the conventional bulky optical devices on small plasmonic chips.

6.7 Acknowledgements

The text of Chapter 6, in part or in full, is a reprint of the material as it appears in the following publication:

Liang Feng, Kevin A. Tetz, Boris Slutsky, Vitaliy Lomakin, and Yeshaiahu Fainman, "Fourier plasmonics: Diffractive focusing of in-plane surface plasmon polaritons waves," Applied Physics Letters **91**(8)**,** 081101 (2007).

The dissertation author was the primary researcher and the co-authors listed in this publication directed and supervised the research which forms the basis for this chapter.

Chapter 7   Nanoscale Optical Field Localization by Resonantly Focused Plasmons

7.1 Introduction

Nanoscale field confinement enabled by plasmonic phenomena has great potential to revolutionize many applications in nanophotonics, including bio-sensing, imaging, and magnetic recording . Many metals in the optical frequency regime behave as electron plasmas, which below the plasma resonance frequency are characterized by a negative (real part of) permittivity. This property is equivalent to having a positive quantum mechanical potential as opposed to negative potential corresponding to dielectric materials [119]. Metal-dielectric surfaces can thus support SPPs, which are electromagnetic modes, extending evanescent fields from both sides of the interface [5]. Various schemes using propagating surface plasmon polariton (SPP) waves have been suggested [32, 101, 110-113]. For properly chosen parameters, the effective index of the SPP modes can be considerably higher than the index of the surrounding dielectric media. The thin metallic structures can support high effective index anti-symmetric (short-range) SPP modes and thus strong field localization [114, 115, 120, 121]. However, this is achieved on the expense of an intrinsically high power loss associated with SPP propagation in such high effective index structures, restricting their practical applications. Localized surface plasmons (LSPs), which are associated with collective oscillations of free electrons in a metal particle [5, 42, 122-124], are arguably a better sub-diffraction limited focusing alternative to adiabatic SPPs due to their smaller domain of

confinement. Additional ultra-strong confinement can be achieved using transverse electromagnetic (TEM) fields supported by small gaps between metals [125-127].

7.2 Geometry of resonant nano-focusing-antenna

It is highly desired to have an optical nanostructure that can simultaneously support all focusing mechanisms that we describe above and thus produce a single nano-focusing spot with strong field localization. In this letter, we introduce a novel plasmonic resonant nano-focusing-antenna (RNFA) geometry for efficient field nano-focusing and localization that simultaneously uses three physical mechanisms: LSPs [42], thin metallic wedge localization of SPP with high effective index [114, 115, 120, 121], and TEM field localization [125-127] (see Fig. 7-1). We fabricate the RNFA nanostructure and for the first time experimentally demonstrate sub-diffraction limited focusing with a nanoscale (deep subwavelength) spot size. The LSPs, thin metallic wedge localization, and TEM field localization in RNFA provide ultra-high confinement (on the order of 25 nm), while simultaneously allowing increasing the overall efficiency of the localized fields due to the resonant nature of LSP and associated large stored near-field energy.

Nano-Disk   Thin Metallic Wedge   Nano-Antenna   RNFA
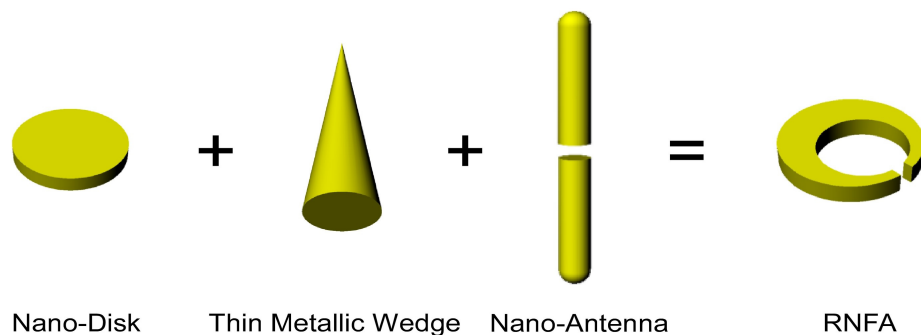
Fig. 7-1. The proposed novel RNFA nanostructure allows simultaneously achieving three optical field localization mechanisms realized with plasmonic phenomena using the corresponding realization geometries: resonant LSPs in nano-disks, thin metallic wedge localization of SPP fields, and TEM field localization in nano-antennas.

LSPs are special electromagnetic eigen modes associated with free electron longitudinal vibrations, exhibiting resonant singularity in spectra such as Mie resonances for small metallic spheres. LSPs on the nano-disk are associated with vibrating electrons on the disk sidewall and they follow the Born-von-Kármárn periodic boundary condition for LSPs that requires that an electron must oscillate in phase after the plasmon wave has experienced an entire round loop. While LSPs on the nano-disk structure already lead to strong field confinement, a significantly smaller field localization spot size can be achieved by introducing the field edge localization by sharpening the nanodisk. The effective index near the sharp edge can be very high (corresponding to a very low potential) thereby resulting in strong plasmonic field localization. The plasmonic fields on two sharp thin metallic wedges of the RNFA in Fig. 7-1 are strongly coupled and they support nearly uniformly distributed TEM type fields regardless of the gap size. These TEM fields are similar to the strong fields obtained at the feed points or small air gaps in dipole, bow-tie, and other small antennas. The gap operates as a capacitor that is known to confine strong fields even in the static regime. Such a nano-capacitor strongly confines the plasmonic fields, already enhanced due to the LSP and the sharp thin metallic wedge localizations.

It should be noticed that though our RNFA geometry looks, in the general shape, similar to the nano-crescent-moon that has been investigated [123, 124], the physics behind our structure is quite different. In all prior work, two edges of the nano-crescent-moon are independent. This discontinuity in the structure actually destroys the continuity of the excited plasmon mode. As a result, the localized surface plasmon resonance in the nano-disk, which is continuous in both structure and plasmon wave mode, *can not be*

reproduced by their nano-crescent-moon. Their nano-crescent-moon is only in the level of the deformation of conventional taper focusing structures (like Refs. 114, 115, 120, 121). Our novel contribution introduces the idea of a dipole wire antenna from microwaves to overcome the issue of the structure discontinuity, and perfectly reproduced the localized surface plasmon resonance in the nano-disk (see Fig. 7-4), thereby simultaneously realizing 3 localization mechanisms. As we mentioned above, the novel focusing effect is drastically enhanced by coexistence of all 3 localizations (the performance can be degraded drastically if one of them is missing). For instance, the intensity of the focusing spot in our RNFA is about 6, 6, and 2 times better compared to the localization spots on a metal nanodisk (see Section 7.4), a nano-crescent-moon (if the same size of the crescent wedge is applied) [123, 124] and a dipole plasmonic nano-antenna [126], respectively. On the other hand, this strong intensity in our RNFA is obtained at only a single spot. Other structures reported in literatures have multiple localization spots, e.g. a dipole plasmonic antenna has two localized spot at its two ends or a nano-disk results in at least two-spots. This obtained functionality is important for applications like sub-diffraction limited confocal microscopy.

7.3 Integration of plasmonics with Si photonics

Our experimental apparatus consists of a lossless Si waveguide integrated with the gold RNFA nanostructure to deliver TE_z-like electromagnetic wave (*x*-polarized light becomes *y*-polarized after the bending area of the waveguide) to the RNFA and excite the LSPs (see Fig. 7-2). To our knowledge, this is the first integration of Si dielectric waveguide with single localized plasmonic element, and this integration provides

interconnection to and from the nanoantenna, enabling unique plasmonic features (like strong field focusing on nanoscale) that are currently unprecedented in conventional Si photonics. The experiments are designed for operation in the near infrared telecommunication optical spectrum range (~1550 nm). Top faces of the RNFA and waveguide are leveled to efficiently excite resonant LSP around the RNFA as well as easily detect the generated LSP outside the Si waveguide using heterodyne near-field scanning optical microscope (H-NSOM) (see insets of Fig. 7-2).
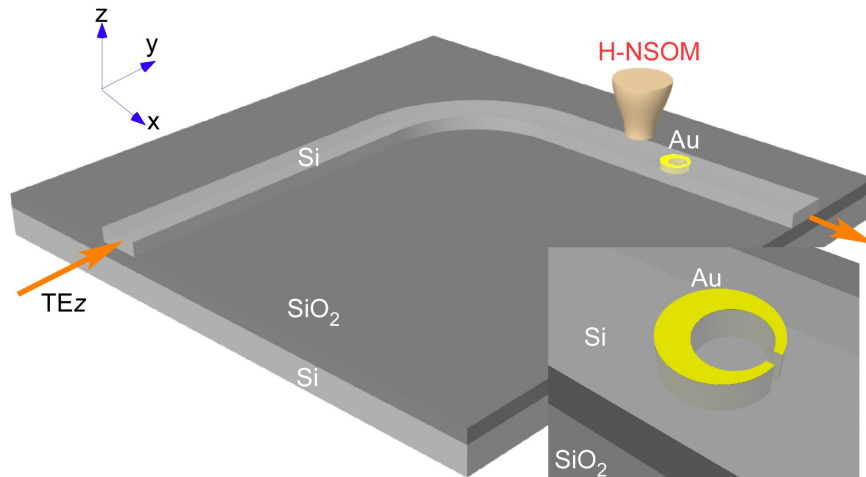
Fig. 7-2. The proposed realization of the experimental setup consisting of monolithically integrated single gold RNFA, placed at the center of a 1 µm-wide Γ-shaped Si waveguide fabricated using SOI technology.

The RNFA sample was fabricated using standard E-beam lithography procedure followed by reactive ion beam etching, gold deposition and focused-ion-beam processing. An SOI wafer with a Si slab thickness of 250 nm and an oxide layer thickness of 3 µm was used to construct the experiment. The Si waveguide was fabricated using the standard E-beam lithography procedure. First, as shown in Fig. 7-3, the designed Si waveguide was fabricated with four alignment marks using the standard E-beam lithography procedure followed by reactive ion etching (RIE) with Chlorine based

chemistry. The second lithography step in fabricating the nano-disks involves spin-coating a 200 nm polymethyl methacrylate (PMMA) onto the entire sample. After the accurate E-beam alignment using the four marks in the Raith50 E-beam Writer, a 250 nm-diameter hole was created in the PMMA mask on the top of the Si waveguide. Chlorine based RIE etching was performed again to etch a 50nm-high cylindrical void in the Si waveguide with PMMA acting as the RIE mask. This cylindrical void was then filled by gold deposition to form the designed gold nano-disk in the Si waveguide. The last fabrication step was performed by using a focused-ion-beam (strata FIB 201, FEI company, 30 keV Ga ions) to make an off-axis cylindrical cut-out and a gap with flat wedges based on the fabricated nanodisk. Finally, the RNFA has been fabricated and placed at the center of a 1 μm-wide Γ-shaped Si waveguide. The diameter and thickness of RNFA are 250 nm and 50 nm, respectively. The center of the 130 nm-diameter cylindrical cut-out is offset from the center of the nano-disk by 40 nm and the gap in the RNFA is only 25 nm (see Fig. 7-5(a)).
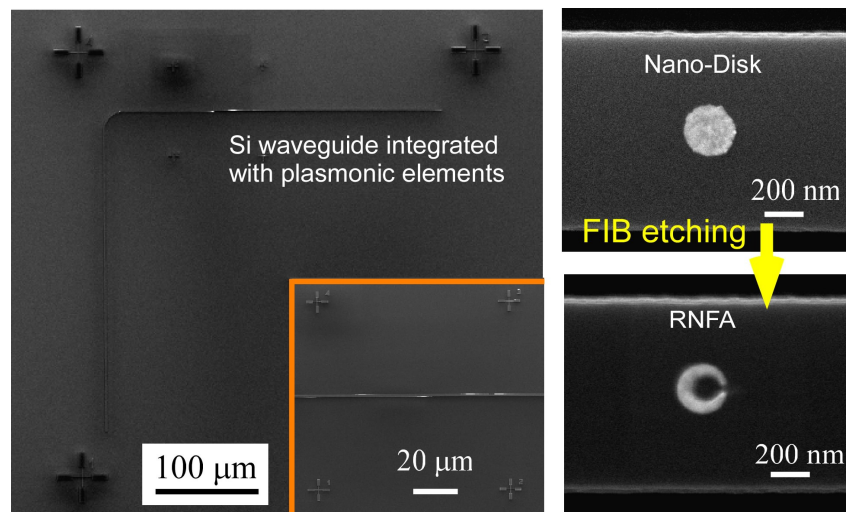
Fig. 7-3. SEM micrographs of the fabricated monolithically integrated experimental system, including a Si waveguide integrated with a plasmonic RNFA. The FIB technique was used to fabricate the small off-centre cylindrical cut-out and the small gap of RNFA from a nano-disk.

7.4 Numerical analysis

Finite element computer simulations with commercial software (Ansoft HFSS v9.0) summarized in Fig. 7-4 are used first to validate our proposed concepts. A comparison between the calculated resonant responses of the electric field intensity (squared magnitude) averaged over the volume defined by half-intensity of the corresponding maximum, which is achieved at the RNFA gap and the LSP localization spots in a simple gold nano-disk, clearly shows about six times resonant enhancement (see Fig. 7-4(a)). Also notice that the averaged intensity in the RNFA gap is enhanced ~2-order of magnitude compared to light inside the Si waveguide.
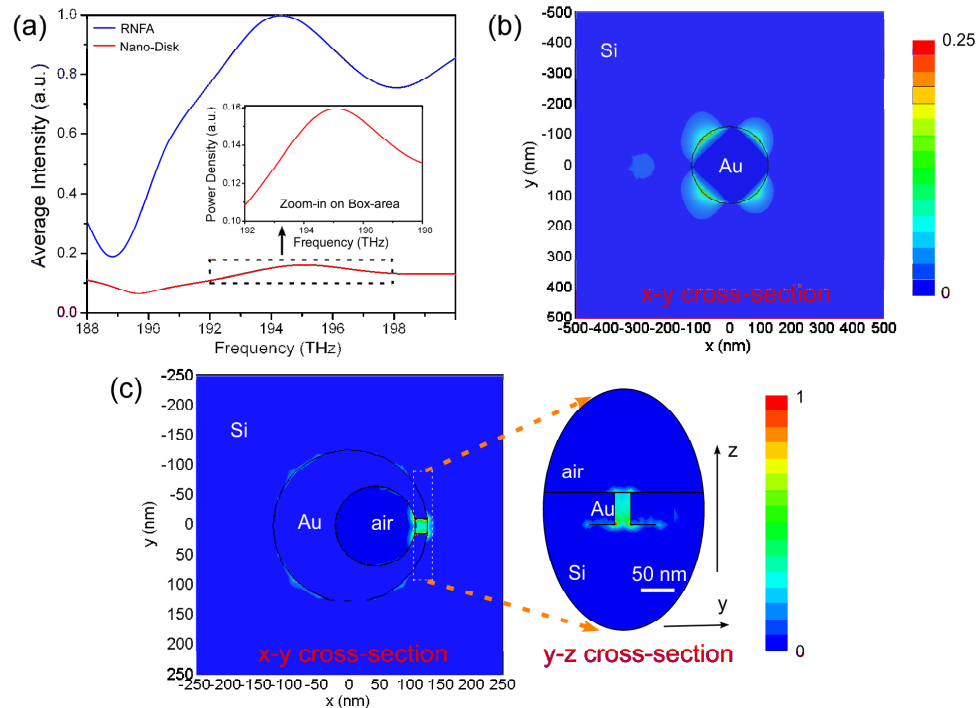
Fig. 7-4. Comparative numerical analysis of LSP resonance on RNFA and nano-disk: (a) The blue and the red curves show the spectra of the average intensities at the gap of the RNFA nanostructure and the field localization regions of the nano-disk, respectively. (b) Map of the LSP electric field intensity distribution on the top surface of the waveguide and nano-disk interface at the resonant frequency of 195 THz (wavelength of 1538.5 nm). c. Map of the electric field intensity distribution around the RNFA-Si interface (left) and the transverse plane cross-section at the center of the gap of the RNFA structure (right) at the resonant frequency of 194.5 THz (wavelength of 1542 nm).

At the resonant frequency, the LSP field is strongly confined at the edge of the nano-disk and decays exponentially. While in Fig. 7-4(c), the field is strongly and uniformly localized inside the nano-capacitor formed by the gap with the spot size of about 25 nm along the *x* direction. Note that the RNFA and nano-disk structures share similar eigen-frequencies and have resemblance in the spatial modal structure. The eigen-frequencies of the LSPs of the two structures are 194.5 THz (wavelength of 1542 nm) for the RNFA and 195 THz (wavelength of 1538.5 nm) for the nano-disk, respectively. The resonant field distributions in Figs. 7-4(b) and 7-4(c) also have similar spatial modal structure consisting of four similar peaks along the circular perimeter corresponding to twice the surface plasmon wavelengths length of the resonator round loop. These similarities between the eigen-states have the same nature as the current distribution in a microwave dipole wire antenna, which is nearly identical to the case of free standing wire and an antenna of the same size fed through a small gap. Due to reciprocity, which is one of the fundamental principles of electromagnetism, the gap does not change significantly the source-excited or source-free field/current distributions as well as eigen-frequencies of such structures.

In other words, the LSP resonance in RNFA can be seen as a "short-circuit" resonance compared to the LSP resonance in nano-disks. The definition of "short- and open-circuit" resonances is given in Ref. 126. The "short-circuit" resonance corresponds to the case where the small gap (the capacitor) is located at the minimum of the electric field in the original nano-disk. Without a gap, the magnetic field is the strongest and the electric field is the weakest at this location (hence the notation "short-circuit"). With the gap placed at this "short-circuit" location, the time variations of the strong magnetic field

lead to a voltage in the gap. The presence of this voltage, however, does not affect significantly the modal field because the gap is small and this effect is local. However, since the gap is small the voltage is transformed into a very strong local electric field between the gap edges just like in a capacitor. As mentioned above, this behavior is of the same nature as in the feed points of many gap fed microwave antennas, e.g. dipole antennas. The optical field impedance values of thin metallic wedges and the small gap associated with this "short-circuit" resonance are close to zero. Thus the impedance value of the entire RNFA geometry is similar to its original nano-disk's [126].

For the open-circuit case, the situation is opposite, i.e. the modal magnetic field is minimal at the gap location. Therefore, the resulting electric field in the gap is weak. The modal electric field still has a maximum, which however is much lower than the strong field enhancement obtained due to the gap field localization.

With the "short-circuit" resonance, the fact that resonant frequencies of the nano-disk and RNFA are close has an important practical implication in relaxing the fabrication tolerance for constructing the RNFA from a nano-disk. Moreover, for the complicated RNFA structure, its eigen-frequencies can be characterized by developing closed form approximate expressions for a simple nano-disk structure. While the LSP field impedance and resonant frequencies do not change, the presence of the sharp thin metallic wedges and the small gap results in more than 6-fold enhancement of the field intensity (see Fig. 7-4(a)) localized in all 3 dimensions inside the nano-capacitor with a 25 nm gap.

7.5 Experimental characterizations

The near field H-NSOM measurements are performed first with a tip scanning step size of 100 nm to locate the resonance by simultaneously scanning the optical frequencies of the input field in the range of 191 THz to 196 THz over a scanning area of 15 μm × 15 μm centered on the RNFA. The data shows a strong LSP localization at the frequency of 194.2 THz (λ_0=1544.9 nm).

The waveguide mode was successfully converted to the highly confined LSP resonance mode in the RNFA (see Fig. 7-5(b)). We can see here that the introduction of our RNFA does not strongly disturb the original waveguide mode as the transmission of the light in the waveguide after RNFA is about 65%, since the height and the size of RNFA are significantly smaller than the waveguide size and the modal extent. Next we use the input optical field at the resonant frequency to detect a high resolution near field intensity map with H-NSOM tip scanning step size of 10 nm (see Fig. 7-5(c)). The strong field localization obtained experimentally in Fig. 7-5(c) corresponds to the resonance of LSPs on the RNFA. The measured spot size along the x direction taking into account the finite probe aperture size was about 220 nm. Since the expected nanofocusing spot size is only tens of nanometers (corresponding to the size of the nano-capacitor), the measurement of the actual size even with current H-NSOM techniques is challenging owing to the size and the electromagnetic interaction between the probe and the measured structure. We consider these near field interaction effects in the RNFA characterization experiments by including a deconvolution procedure into our H-NSOM process (see Section 7.7). In the a restored near field intensity image shown in Fig. 7-5(d), the estimated effect of the probe on the convolution with the measured localized optical field

is an effective aperture of about 155±5 nm, consistent with the estimates achieved for other plasmonic nanostructures we tested in H-NSOM measurement (e.g. 150 nm for nanodisks). An elliptical focusing spot was obtained, which is associated with a slightly weaker localization in the y direction. The field localization along the x direction estimated from the restored measured data in Fig. 7-5(d) is about 75±5 nm.
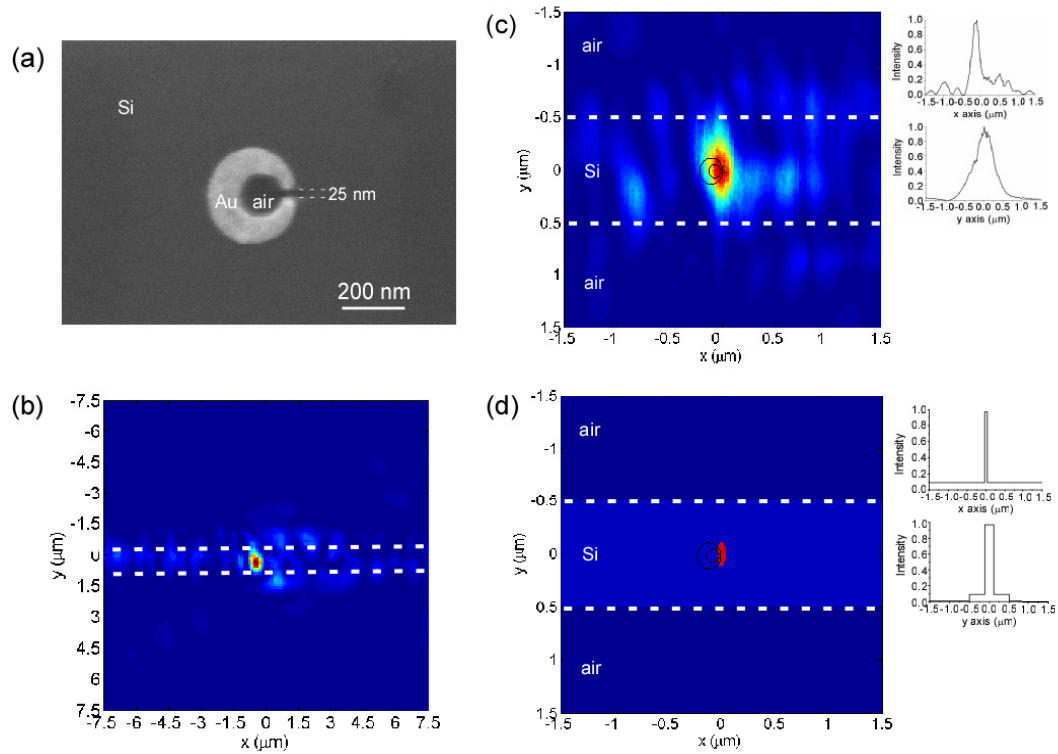
Fig. 7-5. Experimental results on characterization of the optical field localization in resonant RNFA geometry. (a) SEM micrograph of the RNFA geometry. (b) Low resolution H-NSOM field intensity at the frequency of 194.2THz (wavelength of 1544.9 nm). The bright spot in the middle of the waveguide (see dotted line) corresponds to the highly confined LSP modes in RNFA. (c) Raw H-NSOM image of high resolution intensity mapping measured at 194.2 THz. (d) Processed image of the field intensity in the same area after deconvolution signal processing to extract the effect of the NSOM probe on the measured data. Insets of (c) and (d) show the cross-section data along the *x* (top) and *y* (bottom) axis. The RNFA shaped sketch in (c) and (d) indicates the position of the RNFA geometry.

As shown in Fig. 7-4(a), the Quality factor of our RNFA is determined by the original nano-disk and is typically about 10. Thus the intensity as well as field

distribution varies relatively slowly with different wavelengths. This means that, within the range we did the simulation and measurement, the field distribution on the structure is very similar (strong focusing spot in the gap and other 4 bright spots on the sidewall can be obtained) but the coupling efficiency is slightly lower for off-resonant excitation. For example, at the wavelength of 192.3 THz (λ_0=1560 nm) the measurement results show that the contrast of the focusing spot to the incident waveguide mode is about twice lower than that under the resonant excitation in Fig. 7-5(c).

7.6 Conclusions

The RNFA geometry has been analyzed theoretically and demonstrated experimentally to efficiently convert a waveguide mode into a resonant LSP mode, which is localized into an extraordinary small volume of deep subwavelength size on nanoscale. In principle, the size of the localization is only determined by the size of the RNFA's gap. Such strong field localization is obtained due to combined effects of the resonant LSPs, edge localization by the sharp thin metallic wedges, and TEM field localization in the gap nano-capacitor. The presented structure and phenomena are anticipated to have important impacts on many applications including constructing novel devices for bio-medical imaging, bio-sensing, nano-lithography, heat-assisted magnetic recording, and plasmonic nanocircuits operating at optical frequencies. In addition, our integration of conventional Si photonics (e. g., Si waveguides) with plasmonic elements will also help to further advance incorporating unique unprecedented functionalities enabled by plasmonic devices into Si photonics.

7.7 Appendix- Deconvolution procedure

Once the aperture of H-NSOM's probe is comparable or bigger than the size of the localized optical field, the experimentally measured spot size is affected by the tip size and its interference with the plasmonic nanostructure. To estimate the size of the plasmonic localization, we need to perform measured data post-processing.
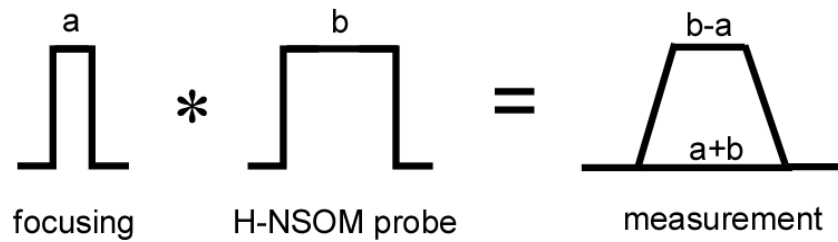
Fig. 7-6. Description of the digital post-processing deconvolution process to estimate the size of the localized field spot size from the measured data.

For simplicity, we consider a 1-dimensional case and make an assumption that the impulse response functions for both the localized field being characterized and the probe aperture of the H-NSOM have shapes of rect(x/a) and rect(x/b) functions with their corresponding widths of a and b, respectively. The result of the convolution between such two rectangular functions produces a trapezoid shape (see Fig. 7-6), representing an approximation to the measured data. The widths of this trapezoid's bases are $b-a$ and $a+b$, respectively, and both of them can be retrieved from the measured data obtained in the experiments. Hence, the actual focusing and the probe effect can be retrieved once the trapezoid shape is established.

To find the trapezoid shape from the measured data (see Fig. 7-5(c)), we first perform a Gaussian fit with minimum variance. The intuition of the Gaussian fitting can be viewed as first finding a Gaussian-shaped bounded stripe area that tightly wraps the

data inside and then choose the center contour of this stripe as the fitting result. Hence, it should be statistically reasonable to take the peak value as the average of the data within the central region [128]. The peak value of the Gaussian fit was thus chosen as the upper base of the trapezoid. The linear fit was performed twice on the Gaussian curve separately, before and after the peak, to obtain two sides of the trapezoid. Fig. 7-7 shows the raw data along the x direction (extracted from Fig. 7-5(c)) and the corresponding trapezoidal fits with minimum variance for the RNFA.
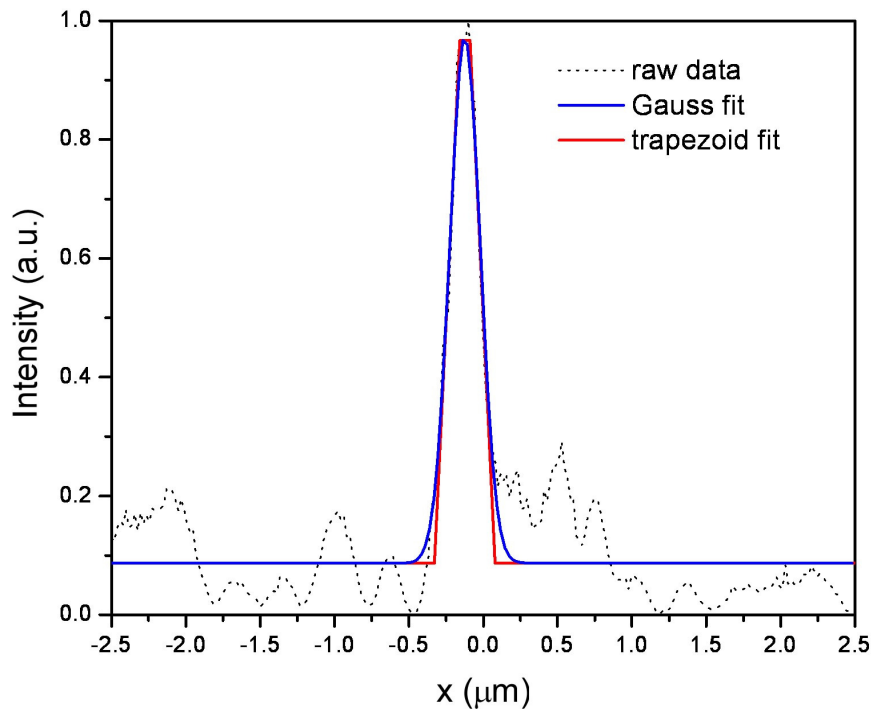
Fig. 7-7. Intensity distributions of the measured experimental data along the x direction determined from Fig. 7-5(c) for RNFA. A trapezoidal fit (red) is performed to a Gaussian fit (blue) of the measured data (black dotted).

This trapezoidal fit was performed 4 times for measured data from Fig. 7-5(c) along the x, y, xy and $-xy$ directions. The 1-dimensional estimates along these directions are used to approximate the 2-dimensional field in the x-y plane similar to that in Fig. 7-

5(c). The retrieved widths of the localized field spot sizes from these 4 trapezoids along the 4 directions corresponding directions were used to create a fit by an ellipse in *x-y* plane using minimum variance criterion.

We call this procedure deconvolution process. The resulting ellipse represents the estimated restored local field spot size and is used to calculate the fields in Figs. 7-5(d).

7.8 Acknowledgements

The text of Chapter 7, in part or in full, is a reprint of the material as it appears in the following publication:

The dissertation author was the primary researcher and the co-authors listed in this publication directed and supervised the research which forms the basis for this chapter.

Chapter 8 Conclusions

8.1 Summary

This dissertation presents the investigation of chip-scale resonant plasmonic nanostructures, in order to manipulate light on the plasmonic chips from nano to micro scales. These plasmonic nanostructures are expected to become crucial building blocks in future miniaturized and integrated photonic devices and systems.

The contribution of each chapter was addressed as follows. In Chapter 3, we presented the analysis of properties of a deep subwavelength metallic grating and investigated its associated plasmonic responses. The 2D metallic grating engineered on the nanoscale acts as an effective uniaxial birefringent metal and exhibits a strong in-plane plasmonic anisotropy. This anisotropic birefringent plasmonic metamaterial establishes its optical plasmonic anisotropy as its SPP index ellipsoid is directly observed in experiments. In addition, our work shows possibilities of adapting more complex Bravais crystal lattices and thus realizing a bi or multi-axial anisotropic metal for more complicated plasmonic manipulation. These plasmonic metamaterials demonstrate an approach to construct important plasmonic devices on-a-chip, such as polarizers and waveplates for SPPs.

In Chapter 4, we demonstrate both theoretically and experimentally a novel and original physical phenomenon, namely, that a TE incident field may excite a surface plasmon wave with efficiency of virtually 100%. This discovery is counterintuitive and expected to be of great interest and surprise to a large audience of scientists. To achieve this goal of breaking down the TM excitation barrier, we use the first optical designer

plasmonic metamaterial in visible light frequencies. The experimental realization is performed using advanced nanofabrication techniques and a unique characterization method. Both simulations and experiments show that the highly efficient TE coupling occurs for a surprisingly broad band of optical frequencies. We believe that this breakthrough discovery can drastically impact a large variety of plasmonic applications, such as plasmon-assisted photovoltaic energy conversion, sensing and detection. We also expect that this work will open the door to a new type of nanoscale metamaterials. By utilizing the concepts presented in Chapter 4, one may be able to engineer sophisticated three dimensional deep subwavelength structures for both microscopic and macroscopic polarization manipulation that will allow controlling the coupling of different guided waves, as well as the coupling of guided waves to free space beams.

In Chapters 5 and 6, we demonstrate the feasibilities of integrating and miniaturizing conventional bulky free-space optical devices on plasmonic chips, such as photonic crystals and diffractive optical components. In Chapter 5, we first analyze theoretically the optimized conditions to achieve a complete bandgap with a 2D plasmonic photonic crystal. The fabricated device was then characterized using our far-field SPP imaging technique, experimentally confirming the designed band structure. In Chapter 6, we present an in-plane Fresnel zone plate (FZP) for focusing SPP fields designed by Fourier plasmonics on the scale of tens of microns. Diffracted SPP fields from each Fresnel zone constructively interfere at the expected focal point to produce focusing with 3-fold intensity enhancement. The experimental results are consistent with the theoretical calculations using the conventional Fourier optics.

In Chapters 6 and 7 we discussed the approach of strongly focusing light using SPPs. Besides the diffractive focusing of in-plane propagating SPPs using the FZP designed by Fourier plasmonics in Chapter 6, we proposed in Chapter 7 a novel localized plasmonic geometry, to achieve a sub-diffraction limited focusing with a nanoscale (deep subwavelength) spot size. The plasmonic resonant nano-focusing-antenna (RNFA) simultaneously supports several focusing mechanisms in a single nanostructure and therefore drastically improves the coupling efficiency of the strongly localized optical fields. The metallic RNFA is integrated with a lossless Si waveguide and effectively converts an incoming propagating waveguide mode to a localized resonant plasmon mode in an ultrasmall volume in all 3 dimensions. This plasmonic nanoscale field localization is finally characterized and validated by the heterodyne near-field scanning optical measurements.

8.2 Future directions

During the last few years, the research field of plasmonics is rapidly growing, as these structures are expected to become crucial building blocks in large variety of optical devices and systems. In the following we are briefly describe the potential areas of the applications that would benefit from such structures.

A. Gain-assisted plasmonics

Metals near the plasma frequency are inherently associated with an energy dissipation caused by the imaginary part of the dielectric constant, leading to significant loss to the propagating SPPs. A possible solution to this problem is to incorporate dielectric gain materials to compensate the material loss due to metals [129]. Furthermore,

the spontaneous emission rate of the gain material can be drastically enhanced, if covered by plasmonic structures, due to the small plasmonic optical volume [13, 14, 130]. The gain coefficient can thus be expected to be much larger than that in bulk gain materials, which is in principle possible to create a lossless SPP propagation. In this thesis, we have demonstrated various schemes to achieve optical filed localizations. Therefore, in the future, we would like to apply these schemes with gain material to realize lossless SPPs as well as nanoscale plasmonic lasing.

B. Surfaced enhanced nonlinear optics

Multiple-wave mixing processing occurs, as the amplitudes of the local electric fields become so large that in a highly polarizable nonlinear medium the nonlinear optical interactions where the photons interact with each other are pronounced. The electromagnetic fields of SPPs are strongly enhanced by the orders of magnitude, and conversion efficiencies of nonlinear processes can be increased dramatically as nonlinear materials are located on the surfaces of plasmonic structures, such as surface enhanced Raman scattering. In the future, the research would cover the development of methods to design the plasmonic structure to satisfy the phase matching and the resonance conditions for each of the involved frequencies. We should also develop the simulation tools to calculate the nonlinear effect for the multiple-plasmonic resonant structures, as well as fabrication and characterization of techniques to demonstrate the concepts and the designed devices.

C. Super-resolution imaging

Light emitted or scattered from an object includes not only propagating waves but also evanescent waves that carry the subwavelength detail of the object. The evanescent

waves usually decay exponentially and can not propagate. However, with SPPs, evanescent waves can be efficiently coupled into surface modes and enhanced by their resonant nature when their wave vectors are matched. Therefore, with SPPs, it is possible to realize super-resolution imaging and resolve the subwavelength information of the object. In addition, the "hot spots" created by plasmonic field localization in Chapters 6 and 7 can be used as a focusing spot in confocal microscopy. The resolution of the confocal microscopy is determined by the size of the "hot spot" that is on the order of nanometers. In the future, these plasmonic assisted super-resolution imaging techniques can be applied to bio-chemical imaging and detection for analysis of dynamics of bio-molecules on nanoscale.

References

[1] V. R. Almeida, C. A. Barrrios, R. R. Panepucci, and M. Lipson, "All-optical control of light on a silicon chip," Nature **431**(7012),1081-1084 (2004).

[2] K. J. Vahala, "Optical microcavities," Nature **424**(6950), 839-846 (2003).

[3] J. S. Foresi, P. R. Villeneuve, J. Ferrera, E. R. Thoen, G. Steinmeyer, S. Fan, J. D. Joannopoulos, L. C. Kimerling, H. I. Smith, and E. P. Ippen, "Photonic-bandgap microcavities in optical waveguides," Nature **390**(6656), 143-145 (1997).

[4] T. A. Klar, S. Jakobs, M. Dyba, A. Egner, and S. W. Hell, "Fluorescence microscopy with diffraction resolution limit broken by stimulated emission," Proc. Natl. Acad. Sci. USA **97**(15), 8206-8210 (2000).

[5] H. Raether, *Surface Plasmons on Smooth and Rough Surfaces and on Gratings* (Springer-Verlag, 1988).

[6] K. A. Willets and R. P. Van Duyne, "Localized surface plasmon resonance spectroscopy and sensing," Annu. Rev. Phys. Chem. **58**, 267-297 (2007).

[7] L. Pang, G. Hwang, B. Slutsky, and Y. Fainman, "Spectral sensitivity of two-dimensional nanohole array surface plasmon polariton resonance sensor," Appl. Phys. Lett. **91**(12), 123112 (2007).

[8] J. R. Pendry, "Negative refraction makes a perfect lens," Phys. Rev. Lett. **85**(18), 3966-3999 (2000).

[9] N. Fang, H. Lee, C. Sun, and X. Zhang, "Sub-diffraction-limited optical imaging with a silver superlens," Science **308**(5721), 534-547 (2005).

[10] Z. Liu, H. Lee, Y. Xiong, C. Sun, and X. Zhang, "Far-field optical hyperlens magnifying sub-diffraction-limited objects," Science **315**(5819), 1686 (2007).

[11] S. Kawata, A. Non, and P. Verma, "Subwavelength colour imaging with a metallic nanolens," Nature Photon. **2**(7), 438-442 (2008).

[12] D. J. Bergman and M. I. Stockman, "Surface plasmon amplification by stimulated emission of radiation: Quantum generation of coherent surface plasmons in nanosystems," Phys. Rev. Lett. **90**(2), 027402 (2003).

[13] M. A. Noginov, G. Zhu, A. M. Belgrave, R. Bakker, V. M. Shalaev, E. E. Narimanov, S. Stout, E. Herz, T. Suteewong, and U. Wiesner, "Demonstration of a spaser-based nanolaser," Nature **460**(7259), 1110-1112 (2009).

[14] R. F. Oulton, V. J. Sorger, T. Zentgraf, R. M. Ma, C. Gladden, L. Dai, G. Bartal, and X. Zhang, "Plasmon lasers at deep subwavelength scale," Nature **461**(7264), 629-632 (2009).

[15] L. Cao, J. S. White, J. S. Park, J. A. Schuller, B. M. Clemens, and M. L. Brongersma, "Engineering light absorption in semiconductor nanowire devices," Nature Mater. **8**(8), 643-647 (2009).

[16] W. Srituravanich, L. Pan, Y. Wang, C. Sun, D. B. Bogy, and X. Zhang, "Flying plasmonic lens in the near field for high-speed nanolithography," Nature Nanotech. **3**(12), 733-737 (2008).

[17] P. Zijlstra, J. W. M. Chon, and M. Gu, "Five-dimensional optical recording mediated by surface plasmons in gold nanorods," Nature **459**(7245), 410-413 (2009).

[18] W. Srituravanich, N. Fang, C. Sun, Q. Luo, and X. Zhang, "Plasmonic nanolithography," Nano Lett. **4**(6), 1085-1088 (2004).

[19] W. A. Challener, T. W. McDaniel, C. D. Mihalcea, K. R. Mountfield, K. Pelhos, and I. K. Sendur, "Light delivery techniques for heat-assisted magnetic recording," Jpn. J. Appl. Phys. **42**(2B), 981-988 (2003).

[20] W. A. Challener, C. Peng, A. V. Itagi, D. Karns, W. Peng, Y. Peng, X. Yang, X. Zhu, N. J. Gokemeijer, Y. T. Hsia, G. Ju, R. E. Rottmayer, M. A. Seigler, and E. C. Gage, "Hear-assisted magnetic recording by a near-field transducer with efficient optical energy transfer," Nature Photon. **3**(4), 220-224 (2009).

[21] N. Ashcroft and N. Mermin, *Solid State Physics* (Brooks Cole, 1976).

[22] R. H. Ritchie, "Plasma losses by fast electrons in thin films," Phys. Rev. **106**(5), 874-881 (1957).

[23] H. Raether, *Excitation of Plasmons and Interband Transitions by Electrons*, vol. 88 of *Springer Tracts in Modern Physics* (Springer, Berlin, Heidelberg, New York, 1980).

[24] E. Kretschmann and H. Raether, "Radiative decay of nonradiative surface plasmons excited by light," Z. Naturforsch. A **23**, 2135-2136 (1968).

[25] A. Otto, "Excitation of nonradiative surface plasma waves in silver by the method of frustrated total reflection," Z. Phys. **216**, 398 (1968).

[26] B. Hecht, H. Bielefeldt, L. Novotny, Y. Inouye, and D. W. Pohl, "Local excitation, scattering, and interference of surface plasmons," Phys. Rev. Lett. **77**(9), 1889-1892 (1996).

[27] Z. Liu, N. Fang, T. J. Yen, and X. Zhang, "Rapid growth of evanescent wave by a silver superlens," Appl. Phys. Lett. **83**(25), 5184-5186 (2003).

[28] R. H. Ritchie, E. T. Arakawa, J. J. Cowanand, and R. N. Hamm, "Surface-plasmon resonance effect in grating diffraction," Phys. Rev. Lett. **21**(22), 1530-1533 (1968).

[29] B. Rothenhausler, J. Rabe, P. Korpiu, and W. Knoll, "On the decay of plasmon surface polaritons at smooth and rough Ag-air interfaces: A reflectance and photo-acoustic study," Surf. Sci **137**(1), 373-383 (1984).

[30] T. W. Ebbesen, H. J. Lezec, H. F. Ghaemi, T. Thio, and P. A. Wolff, "Extraordinary optical transmission through sub-wavelength hole arrays," Nature **391**(6668), 667-669 (1998).

[31] K. A. Tetz, R. Rokitski, M. Nezhad, and Y. Fainman, "Excitation and direct imaging of surface plasmon polariton modes in a two-dimensional grating," Appl. Phys.Lett. **86**(11), 111110 (2005).

[32] R. Rokitski, K. A. Tetz, and Y. Fainman, "Propagation of femtosecond surface plasmon polariton pulses on the surface of a nanostructured metallic file: space-time complex amplitude characterization," Phys. Rev. Lett. **95**(17), 177401 (2005).

[33] H. Liu and P. Lalanne, "Microscopic theory of the extraordinary optical transmission," Nature **452**(7188), 728-731 (2008).

[34] W. L. Barnes, A. Dereux, and T. W. Ebbesen, "Surface plasmon subwavelength optics," Nature **424**(6950), 824-830 (2003).

[35] L. Martin-Moreno, F. J. Garcia-Vidal, H. J. Lezec, K. M. Pellerin, T. Thio, J. B. Pendry, and T. W. Ebbesen, "Theory of extraordinary optical transmission through subwavelength hole arrays," Phys. Rev. Lett. **86**(6), 1114-1117 (2001).

[36] W. L. Barnes, W. A. Murray, J. Dintinger, E. Devaux, and T. W. Ebbesen, "Surface plasmon polaritons and their role in the enhanced transmission of light through periodic arrays of subwavelength holes in a metal film," Phys. Rev. Lett. **92**(10), 107401 (2004).

[37] H. J. Lezec, A. Degiron, E. Devaux, R. A. Linke, L. Martin-Moreno, F. J. Garcia-Vidal, and T. W. Ebbesen, "Beaming light from a subwavelength aperture," Science **297**(5582), 820-822 (2002).

[38] Q. Cao and P. Lalanne, "Negative role of surface plasmons in the transmission of metallic gratings with very narrow slits," Phys. Rev. Lett. **88**(5), 057403 (2002).

[39] Z. Ruan and M. Qiu, "Enhanced transmission through periodic arrays of subwavelength holes: The role of localized waveguide resonances," Phys. Rev. Lett. **96**(23), 233901 (2006).

[40] K. J. Klein Koerkamp, S. Enoch, F. B. Segerink, N. F. Van Hulst, and L. Kuipers, "Strong influence of hole shape on extraordinary transmission through periodic arrays of subwavelength holes," Phys. Rev. Lett. **92**(18), 183901 (2004).

[41] R. H. Ritche and J. Crowell, "Radiative decay of Coulomb-stimulated plasmons in spheres," Phys. Rev. **172**(2), 436-440 (1968).

[42] E. Hutter and J. H. Fendler, "Exploitation of localized surface plasmon resonance," Adv. Mater. **16**(19), 1685-1706 (2004).

[43] F. Fujimoto and K. Komaki, "Plasma oscillations excited by a fast electron in a metallic particle," J. Phys. Soc. Jpn. **25**(6), 1679-1687 (1968).

[44] S. Nie and S. R. Emory, "Probing single molecules and single nanoparticles by surface-enhanced raman scattering," Science **275**(5303), 1102-1106 (1997).

[45] A. Fujiki, T. Uemura, N. Zettsu, M. Akai-Kasaya, A. Saito, and Y. Kuwahara, "Enhanced fluorescence by surface plasmon coupling of Au nanoparticles in an organic electroluminescence diode," Appl. Phys. Lett. **96**(4) 043307 (2010).

[46] J. I. Gersten and A. Nitzan, "Electromagnetic theory of enhanced Raman scattering by molecules adsorbed on rough surfaces," J. Chem. Phys. **73**(7), 3023-3037 (1980).

[47] P. F. Liao and A. Wokaun, "Lighting rod effect in surface enhanced Raman scattering," J. Chem. Phys. **76**(1), 751-752 (1982).

[48] S. A. Maier, P. G. Kik, H. A. Atwater, S. Meltzer, E. Harel, B. E. Koel, and A. A. G. Requicha, "Local detection of electromagnetic energy transport below the diffraction limit in metal nanoparticle plasmon waveguides," Nature Mater. **2**(4), 229-232 (2003).

[49] S. A. Maier, M. L. Brongersma, and H. A. Atwater, "Electromagnetic energy transport along arrays of closely spaced metal rods as analogue to plasmonic devices," Appl. Phys. Lett. **78**(1), 16-18 (2001).

[50] V. Lomakin, M. Lu, and E. Michielssen, "Optical wave properties of nano-particle chains coupled with a metal surface," Opt. Express **15**(19) 11827-11842 (2007).

[51] S. Wang, D. F. P. Pile, S. Sun, and X. Zhang, "Nanopin plasmonics resonator array and its optical properties," Nano Lett. **7**(4), 1076-1080 (2007).

[52] J. B. Pendry, A. J. Holden, D. J. Robbins, and W. J. Stewart, "Magnetism from conductors and enhanced nonlinear phenomena," IEEE Tran. Micro. Theory & Tech. **47**(11), 2075-2084 (1999).

[53] D. R. Smith, W. J. Padilla, D. C. Vier, S. C. Nemat-Nasser, and S. Schultz, "Composite medium with simultaneously negative permeability and permittivity," Phys. Rev. Lett. **84**(18), 4184-4187 (2000).

[54] T. J. Yen, W. J. Padilla, N. Fang, D. C. Vier, D. R. Smith, J. B. Pendry, D. N. Basov, and X. Zhang, "Terahertz magnetic response from artificial materials," Science **303**(5663), 1494-1496 (2004).

[55] S. Linden, C. Enkrich, M. Wegener, J. Zhou, T. Koschny, and C. M. Soukoulis, "Magnetic response of metamaterials at 100 Terahertz," Science **306**(5700), 1351-1353 (2004).

[56] V. M. Shalaev, W. Cai, U. K. Chettiar, H. K. Yuan, A. K. Sarychev, V. P. Drachev, and A. V. Kildishev, "Negative index of refraction in optical metamaterials," Opt. Lett. **30**(24), 3356-3358 (2005).

[57] A. N. Grigorenko, A. K. Geim, H. F. Gleeson, Y. Zhang, A. A. Firsov, I. Y. Khrushchev, and J. Petrovic, "Nanofabricated media with negative permeability at visible frequencies," Nature **438**(7064), 17-20 (2005).

[58] R. A. Shelby, D. R. Smith, and S. Schultz, "Experimental verification of a negative index of refraction," Science **292**(5514), 77-79 (2001).

[59] J. Valentine, S. Zhang, T. Zentgraf, E. Ulin-Avila, D. A. Genov, G. Bartal, and X. Zhang, "Three dimensional optical metamaterial exhibiting negative refractive index," Nature **455**(7211), 376 (2008).

[60] V. Lomakin, Y. Fainman, Y. Urzhumov, and G. Shvets, "Double negative metamaterials in the near infrared and visible refimes based on thin films," Opt. Express **14**(23), 11164-11177 (2006).

[61] Z. Liu, S. Durant, H. Lee, Y. Pikus, N. Fang, Y. Xiong, C. Sun, and X. Zhang, "Far-field optical superlens," Nano Lett. **7**(2), 403-408 (2007).

[62] A. Yariv and P. Yeh, *Optical waves in crystals: Propagation and control of laser radiation* (Wiley and Sons, New York, 2003).

[63] M. Born and E. Wolf, *Principles of optics: electromagnetic theory of propagation interference and diffraction of light* (Cambridge, University Press, 1999).

[64] I. Richer, P. C. Sun, F. Xu, and Y. Fainman, "Design consideration of form birefringent microstructures," Appl. Opt. **34**(12), 2421-2429 (1995).

[65] R. C. Tyan, A. A. Salvekar, H. P. Chou, C. C. Cheng, A. Scherer, F. Xu, P. C. Sun, and Y. Fainman, "Design, fabrication and characterization of form-birefringent multilayer polarizing beam splitter," J. Opt. Soc. Am. A **14**(7), 1627-1636 (1997).

[66] L. Pang, M. Nezhad, U. Levy, C. H. Tsai, and Y. Fainman, "Form birefringence structure fabrication in GaAs by use of SU-8 as dry etching mask," Appl. Opt. **44**(12), 2377-2381 (2005).

[67] F. Xu, R. C. Tyan, P. C. Sun, Y. Fainman, C. C. Cheng, and A. Scherer, "Form-birefringent computer generated holograms," Opt. Lett. **21**(18), 1513-1515 (1996).

[68] U. Levy, M. Abashin, K. Ikeda, A. Krishnamoorthy, J. Cunningham, and Y. Fainman, "Inhomogeneous dielectric metamaterials with space-variant polarizability," Phys. Rev. Lett. **98**(24), 243901 (2007).

[69] S. L. Neale, M. P. MacDonald, K. Dholakia, and T. F. Krauss, "All-optical control of microfluidic components using form-birefringence," Nature Mater. **4**(7), 530-533 (2005).

[70] J. Elser and V. A. Podolskiy, "Scattering-free plasmonic optics with anisotropic metamaterials," Phys. Rev. Lett. **100**(6), 066402 (2008).

[71] S. M. Rytov, "Electromagnetic properties of a finely stratified medium," Sov. Phys. JETP **2**(3), 466-475 (1956).

[72] J. Yao, Z. Liu, Y. Liu, Y. Wang, C. Sun, G. Bartal, A. Stacy, and X. Zhang, "Optical negative refraction in bulk metamaterials," Science **321**(5891), 930 (2008).

[73] J. Elser, R. Wangberg, V. A. Podolskiy, and E. E. Narimanov, "Nanowire metamaterials with extreme optical anisotropy," Appl. Phys. Lett. **89**(26), 261101 (2006).

[74] E. D. Palik, *Handbook of optical constants of solids* (Academic Press, New York, 1985).

[75] W. Cai, U. K. Chettiar, A. V. Kildishev, and V. M. Shalaev, "Optical cloaking with metamaterials," Nature Photon. **1**(4), 224-227 (2007).

[76] J. B. Pendry, L. Martin-Moreno, and F. J. Garcia-Vidal, "Mimicking surface plasmons with structured surfaces," Science **305**(5685), 847-848 (2004).

[77] F. J. Garcia-Vidal, L. Martin-Moreno, and J. B. Pendry, "Surface with holes in them: new plasmonic metamaterials," J. Opt. A: Pure Appl. Opt. **7**(2), S97-S101 (2005).

[78] A. P. Hibbins, B. R. Evans, and J. R. Sambles, "Experimental verification of designer surface plasmons," Science **308**(5772), 670-672 (2005).

[79] M. J. Lockyear, A. P. Hibbins, and J.R. Sambles, "Microwave surface-plasmon-like modes on thin metamaterials," Phys. Rev. Lett. **102**(7), 073901 (2009).

[80] S. A. Maier, S. R. Andrews, L. Martin-Moreno, and F. J. Garcia-Vidal, "Terahertz surface plasmon-polariton propagation and focusing on periodically corrugated metal wires," Phys. Rev. Lett. **97**(17), 176805 (2006).

[81] C. R. Williams, S. R. Andrews, S. A. Maier, A. I. Fernandez-Dominguez, L. Martin-Moreno, and F. J. Garcia-Vidal, "Highly confined guiding of terahertz surface plasmon polaritons on strucutured metals surfaces," Nature Photon. **2**(3), 175-179 (2008).

[82] Q. Gan, Z. Fu, Y. J. Ding, and F. J. Bartoli, "Ultrawide-bandwidth slow-light system based on THz plasmonic graded metallic grating structure," Phys. Rev. Lett. **100**(25), 256803 (2008).

[83] T. Takano and J. Hamasaki, "Propagating modes of a metal-clad-dielectric slab waveguide for integrated optics," IEEE J. Quantum Elec. **8**(2), 206-212 (1972).

[84] J. K. Gansel, M. Thiel, M. S. Rill, M. Decker, K. Bade, V. Saile, G. von Freymann, S. Linden, and M. Wegener, "Gold helix photonic metamaterial as broadband circular polarizer," Science **325**(5947), 1513-1515 (2009).

[85] N. Liu, H. Guo, L. Fu, S. Kaiser, H. Schweizer, and H. Giessen, "Three-dimensional photonic metamaterials at optical frequencies," Nature Mater. **7**(1), 31-37 (2008).

[86] E. Yablonovitch, "Inhibited spontaneous emission in solid-state physics and electronics," Phys. Rev. Lett. **58**(20), 2059-2062 (1987).

[87] S. John, "Strong localization of photons in certain disordered dielectric superlattices," Phys. Rev. Lett. **58**(23), 2486-2489 (2987).

[88] J. D. Joannopoulos, S. G. Johnson, J. N. Winn, and R. D. Meade, *Photonic crystals: molding the flow of light* (Princeton NJ, Princeton University Press, 2008).

[89] O. Painter, R. K. Lee, A. Scherer, A. Yariv, J. D. O'Brien, P. D. Dapkus, and I. Kim, "Two-dimensional photonic band-gap defect mode laser," Science **284**(5421), 1819-1821 (1999).

[90] S. Y. Lin, E. Chow, V. Hietala, P. R. Villeneuve, and J. D. Joannopoulos, "Experimental demonstration of guiding and bending of electromagnetic waves in a photonic crystal," Science **282**(5387), 274-276 (1998).

[91] A. Hohenau, J. R. Krenn, A. L. Stepanov, A. Drezet, H. Ditlbacher, B. Steinberger, A. Leitner and F. R. Aussenegg, "Dielectric optical elements for surface plasmons," Opt. Lett. **30**(8), 893-895 (2005).

[92] B. Steinberger, A. Hohenau, H. Ditlbacher, F. R. Aussenegg, A. Leitner, and J. R. Krenn, "Dielectric stripes on gold as surface plasmon waveguide: Bends and directional couplers," Appl. Phys. Lett. **91**(8), 081111 (2006).

[93] L. Feng, K. A. Tetz, B. Slutsky, V. Lomakin and Y. Fainman, "Fourier plasmonics: Diffractive focusing of in-plane surface plasmon polaritons waves," Appl. Phys. Lett. **91**(8), 081101 (2007).

[94] R. Zia and M. L. Brongersma, "Surface plasmon polaritons analogue to Young's double-slit experiment," Nature Nanotech. **2**(7), 426 (2007).

[95] S. I. Bozhevolnyi, J. E. Erland, K. Leosson, P. M. W. Skovgaard, and J. M. Hvam, "Waveguiding in surface plasmon polariton band gap structures," Phys. Rev. Lett. **86**(14), 3008-3011 (2001).

[96] C. Marquart, S. I. Bozhevolnyi and K. Leosson, "Near-field imaging of surface plasmon-polariton guiding in band gap structures at telecom wavelengths," Opt. Express **13**(9), 3303-3309 (2005).

[97] M. U. Gonzalez, J. C. Weeber, A. L. Baudrion, A. Dereux, A. L. Stepanov, J. R. Krenn, E. Devaux, and T. W. Ebbesen, "Deisgn, near-field characterization, and modeling of 45° surface-plasmon Bragg mirrors," Phys. Rev. B **73**(15), 155416 (2006).

[98] J. C. Weeber, A. Bouhelier, G. Colas des Francs, L. Markey, and A. Dereux, "Submicrometer in-plane integrated surface plasmon cavities," Nano Lett. **7**(5), 1352-1359 (2007).

[99] K. M. Ho, C. T. Chan, and C. M. Soukoulis, "Existence of a photonic gap in periodic dielectric structures," Phys. Rev. Lett. **65**(25), 3152-3155 (1990).

[100] X. Zhang, Z. Q. Zhang, L. M. Li, C. Jin, D. Zhang, B. Man, and B. Cheng, "Enlarging a photonic band gap by using insertion," Phys. Rev. B **61**(3), 1892-1897 (2000).

[101] L. Feng, X. P. Liu, Y. F. Tang, Y. F. Chen, J. Zi, S. N. Zhu, and Y. Y. Zhu, "Tunable negative refraction in a two-dimensional active magneto-optical photonic crystal," Phys. Rev. B **71**(19), 195106 (2005).

[102] I. EI-Kady, M. M. Sigalas, R. Biswas, K. M. Ho, and C. M. Soukoulis, "Metallic photonic crystals at optical wavelengths," Phys. Rev. B **62**(23), 15299-15302 (2000).

[103] H. Kosaka, T. Kawashima, A. Tomita, M. Notomi, T. Tamamura, T. Sato, and S. Kawakami, "Superprism phenomena in photonic crystals," Phys. Rev. B **58**(16), 10096-10099(R) (1998).

[104] H. Kosaka, T. Kawashima, A. Tomita, M. Notomi, T. Tamamura, T. Sato, and S. Kawakami, "Self-collimating phenomena in photonic crystals," Appl. Phys. Lett. **74**(9), 1212-1214 (1999).

[105] E. Cubukcu, K. Aydin, E. Ozbay, S. Foteinopoulou and C. M. Soukoulis, "Negative refraction by photonic crystals," Nature **423**(6940), 604-605 (2003).

[106] S. I. Bozhevolnyi, V. S. Volkov, E. Devaux, J.-Y. Laluet, and T. W. Ebbesen, "Channel plasmon subwavelength waveguide components including interferometers and ring resonators," Nature **440**(7083), 508-511 (2006).

[107] V. S. Volkov, S. I. Bozhevolnyi, E. Devaux, J.-Y. Laluet, and T. W. Ebbesen, "Wavelength selective nanophotonics components utilizing channel plasmon polaritons," Nano Lett. **7**(4), 880-884 (2007).

[108] I. I. Smolyaninov, J. Elliott, A. V. Zayats, and C. C. Davis, "Far-field optical microscopy with a nanometer-scale resolution based on the in-plane image magnification by surface plasmon polaritons," Phys. Rev. Lett. **94**(5), 057401 (2005).

[109] I. I. Smolyaninov, Y.-J. Hung, and C. C. Davis, "Magnifying superlens in the visible frequency range," Science **315**(5819), 1699-1701 (2007).

[110] Z. Liu, J. M. Steele, W. Srituravanich, Y. Pikus, C. Sun, and X. Zhang, "Focusing surface plasmons with a plasmonic lens," Nano Lett. **5**(9), 1726-1729 (2005).

[111] Z. Liu, J. M. Steele, H. Lee, and X. Zhang, "Tuning the focus of a plasmonic lens by the incident angle," Appl. Phys. Lett. **88**(17), 171108 (2006).

[112] L. Yin, V. K. Vlasko-Vlasov, J. Pearson, J. M. Hiller, J. Hua, U. Welp, D. E. Brown, and C. W. Kimball, "Subwavelength focusing and guiding of surface plasmons," Nano Lett. **5**(7), 1399-1402 (2005).

[113] R. Kiyan, C. Reinhardt, S. Passinger, A. L. Stepanov, A. Hohenau, J. R. Krenn, and B. N. Chichkov, "Rapid prototyping of optical components for surface plasmon polaritons," Opt. Express **15**(7), 4205-4215 (2007).

[114] M. I. Stockman, "Nanofocusing of optical energy in tapered plasmonic waveguides," Phys. Rev. Lett. **93**(13), 137404 (2004).

[115] E. Verhagen, L. Kuipers, and A. Polman, "Enhanced nonlinear optical effects with a tapered plasmonic waveguide," Nano Lett. **7**(2), 334-337 (2007).

[116] K. Li, X. Li, M. I. Stockman, and D. J. Bergman, "Surface plasmon amplification by stimulated emission in nanolenses," Phys. Rev. B **71**(11), 115409 (2005).

[117] H. Shin and S. Fan, "All-angle negative refraction for surface plasmon waves using a metal-dielectric-metal structure," Phys. Rev. Lett. **96**(7), 073907 (2006).

[118] J. W. Goodman, *Introduction to Fourier Optics*, 2nd ed. (McGraw-Hill, New York, 1996).

[119] R. Hooper, T. W. Preist, and J. R. Sambles, "Making tunnel barriers (including metals) transparent," Phys. Rev. Lett. **97**(5)**,** 053902 (2006).

[120] E. Moreno, S. G. Rodrigo, S. I. Bozhevolnyi, L. Martin-Moreno, and F. J. Garcia-Vidal, "Guiding and focusing of electromagnetic fields with wedge plasmon polaritions," Phys. Rev. Lett. **100**(2)**,** 023901 (2008).

[121] D. K. Gramotnev, D. F. P. Pile, M. W. Vogel, and X. Zhang, "Local electric field enhancement during nanofocusing of plasmons by a tapered gap," Phys. Rev. B **75**(3)**,** 035431 (2007).

[122] C. Langhammer, M. Schwind, B. Kasemo, and I. Zoric, "Localized surface plasmon resonances in aluminum nanodisks," Nano Lett. **8**(5)**,** 1461-1471 (2008).

[123] Y. Lu, G. L. Liu, J. Kim, Y. X. Mejia, and L. P. Lee, "Nanophotonic crescent moon structures with sharp edge for ultrasenstive biomolecular detection by local electromagnetic field enhancement effect," Nano Lett. **5**(1)**,** 119-124 (2005).

[124] M. Cinchetti, A. Gloskovskii, S. A. Nepjiko, G. Schonhense, H. Rochholz, and M. Kreiter, "Photoemission electron microscopy as a tool for the investigation of optical near fields," Phys. Rev. Lett. **95**(4)**,** 047601 (2005).

[125] A. Sundaramurthy, P. J. Schuck, N. R. Conley, D. P. Fromm, G. S. Kino, and W. E. Moerner, "Toward nanometer-scale optical photolithography: utilizing the near-field of bowtie optical nanoantennas," Nano Lett. **6**(3)**,** 355-360 (2006).

[126] P. Muhlschlegel, H.-J. Eisler, O. J. F. Martin, B. Hecht, and D. W. Pohl, "Resonant optical antennas," Science **308**(5728)**,** 1607-1609 (2005).

[127] R A. Alu and N. Engheta, "Input impedance, nanocircuit loading, and radiation tuning of optical nanoantennas," Phys. Rev. Lett. **101**(4), 043901 (2008).

[128] A. Gelman, J. B. Carlin, H. S. Stern, and D. B. Rubin, *Bayesian Data Analysis* (Chapman & Hall/CRC, 2004).

[129] M. P. Nezhad, K. Tetz, and Y. Fainman, "Gain assisted propagation of surface plasmon polaritons on planar metallic waveguides," Opt. Express 12(17), 4072-4079 (2004).

[130] E. M. Purcell, "Spontaneous emission probabilities at radio frequencies," Phys. Rev. 69(11-12), 681 (1946).